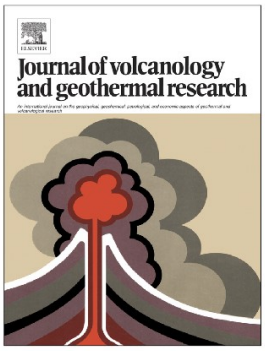

Tectonic constraints on a magmatic plumbing system: The Quetrupillán Volcanic Complex (39°30′ S, 71°43′ W), Southern Andes, Chile

Isla C. Simmons, Joaquín A. Cortés, Dave McGarvie, Eliza S. Calder

PII: S0377-0273(20)30332-2

DOI: https://doi.org/10.1016/j.jvolgeores.2020.107101

Reference: VOLGEO 107101

To appear in: *Journal of Volcanology and Geothermal Research*

Received date: 15 June 2020

Revised date: 6 October 2020

Accepted date: 24 October 2020

Please cite this article as: I.C. Simmons, J.A. Cortés, D. McGarvie, et al., Tectonic constraints on a magmatic plumbing system: The Quetrupillán Volcanic Complex (39°30′ S, 71°43′ W), Southern Andes, Chile, *Journal of Volcanology and Geothermal Research* (2020), https://doi.org/10.1016/j.jvolgeores.2020.107101

Tectonic constraints on a magmatic plumbing system: the Quetrupillán Volcanic Complex (39°30' S, 71°43' W), Southern Andes, Chile

Isla C. Simmons[a]*, Joaquín A. Cortés[a,b], Dave McGarvie[c], Eliza S. Calder[a]

[a] School of GeoSciences, Grant Institute, King's Buildings, University of Edinburgh, Edinburgh, EH9 3FE, UK

[b] Department of Geography, Edge Hill University, St Helens Road, Ormskirk, L39 4QP, UK

[c] Lancaster Environment Centre, Library Avenue, Lancaster University, Lancaster, LA1 4YQ, UK

*Corresponding author: isla.simmons@ed.ac.uk

Other authors: joaquin.cortes@edgehill.ac.uk, d.mcgarvie@lancaster.ac.uk, eliza.calder@ed.ac.uk

Abstract

The Quetrupillán Volcanic Complex is a composite system active since the Pleistocene. We combine petrological and geochemical data from its erupted products with structural and geometrical constraints applied to the overall system and region. We conclude that a basaltic source melt is hindered on its ascent through the crust due to a compressional tectonic regime, influenced further by the structural control imposed by the Liquiñe-Ofqui Fault Zone. The stalled melt evolves by fractional crystallisation within the crust and undergoes a degree of crustal contamination, resulting in a network of trachytic melt pockets within a transcrustal magmatic system. Eruptions sourced from these pockets have generated numerous lava flows with trachytic compositions, which have occurred from the summit and flanks of Quetrupillán during the Holocene. Occasionally, some of the basaltic source melt has reached shallow levels within the plumbing system with minor interaction with the trachytic melt, resulting in the eruption of lavas with basalt, basaltic andesite and trachyandesite compositions. We propose a conceptual model for the magmatic system of Quetrupillán, in which the Liquiñe-Ofqui Fault Zone plays an important role in exerting a structural control on the crust on which Quetrupillán resides, influencing magma residence times and pathways to the surface.

Keywords

Quetrupillán Volcanic Complex; Magmatic plumbing system geometry; Volcano tectonics; Magma mixing; Trachytic melts

1. Introduction

Petrological and geochemical studies allow us to unravel the evolution of magmatic systems, by determining the processes that magmas underwent before eruption at the surface. The textures of

volcanic rocks record their magmatic history (Hersum and Marsh, 2007) and this can provide us with a first-order understanding of the magmatic plumbing system beneath a volcano. Current thinking about volcanic plumbing systems has moved away from the idea of magma chambers as spherical or oblate bodies of liquid magma below volcanoes (Daly, 1911; Marsh, 1989; Gudmundsson, 2012) to transcrustal magmatic systems composed of transient, interconnected lenses of magma within a crystal mush (Cashman et al., 2017; Magee et al., 2018). Partial melting in the mantle supplies basaltic melt and thermal energy to the base of these transcrustal magmatic systems, then the local and regional crustal tectonics influence whether this basaltic magma is able to reach the surface to erupt or whether it would stall within the crust and evolve into more differentiated products (López-Escobar et al., 1995; Cembrano and Lara, 2009). We explore the application of this concept at the Quetrupillán Volcanic Complex (39°30' S, 71°43' W) in the Southern Andes of Chile (Stern et al., 2007) and propose a conceptual model for its plumbing system.

2. Geological Background

2.1. Regional Geological Setting

Subduction of the Nazca Plate below the South American Plate has resulted in the volcanic arc of the Andes along the western edge of South America (Stern, 2004; Stern et al., 2007). The rate and angle of convergence between these plates has varied through time, with alternating periods of rapid and slow convergence, at dextral-oblique or orthogonal angles (Pardo-Casas and Molnar, 1987). Slow convergence from the Late Cretaceous to Early Eocene was followed by a period of rapid convergence during the Late Eocene, before a return to slow convergence (3.5 ± 2.5 cm/yr) during the Oligocene (Pardo-Casas and Molnar, 1987). The current period of fast convergence has been active since 26 Ma (just before the start of the Miocene) with rates of up to 11 cm/yr. Convergence changed from orthogonal to dextral-oblique at 20 Ma (Pardo-Casas and Molnar, 1987; Cembrano et al., 2000).

The Southern Volcanic Zone (SVZ) of the Andes lies between 33° S and 46° S (Figure 1; López-Escobar et al., 1995), coinciding with the subduction of the Juan Fernandez Ridge into the Peru-Chile trench at the northern end and with the subduction of the Chile Rise at the southern end (Stern, 2004; Stern et al., 2007). Beneath the SVZ, the crustal thickness decreases steadily from ~50 km at 33° S to 35 km at 46° S, with a corresponding decrease in elevation of the main cordillera, from 5000 m to less than 2000 m (Stern, 2004; Cembrano and Lara, 2009), and the angle of the subducted Nazca Plate increases from ~20° at the northern end to >25° at the southern end (Stern, 2004).

The dominant tectonic feature of the SVZ is the Liquiñe-Ofqui Fault Zone (LOFZ; Figure 1), a ~1000 km long NNE-trending intra-arc fault system that dominates the tectonics of the region from 38° S to

47° S (Cembrano et al., 1996; Hernandez-Moreno et al., 2014). Transpression caused by the oblique convergence of the Nazca and South American Plates generated the LOFZ (Hervé, 1994; Cembrano et al., 2000), which has acted as a dextral transpressive strike-slip structure for at least the last 6 Ma (Cembrano and Lara, 2009).

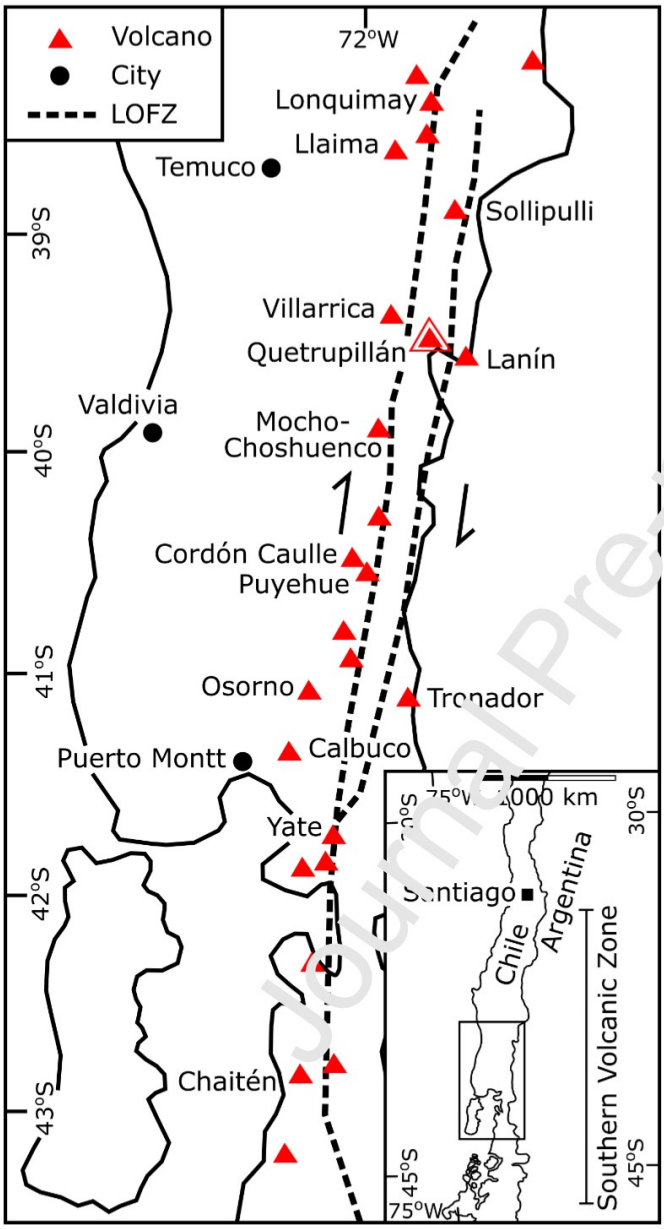

Figure 1: The LOFZ (dashed line) between 38° S and 43.5° S, modified from Cembrano and Lara (2009). The northern terminus of the LOFZ is at 38° S, but it continues for a further ~400 km to the south of this map. Holocene stratovolcanoes are denoted by red triangles and major cities by black circles. Quetrupillán (highlighted) sits between the two main parallel branches of the LOFZ. The inset shows the location of this map and the Southern Volcanic Zone within Chile.

Most Holocene volcanoes are located to the west of the LOFZ (e.g. Llaima, Villarrica, Mocho-Choshuenco and Calbuco). Between ~38.5° S and ~41.5° S the LOFZ splits into two parallel branches (Figure 1; Cembrano and Lara, 2009), and a few volcanoes are located to the east of the eastern branch (e.g. Lanín and Tronador). Quetrupillán is unusual among the volcanoes of the SVZ as it is one of only two stratovolcanoes that lie between the two main branches of the LOFZ (the other being Sollipulli), though several stratovolcanoes appear to lie above or very close to the main trace of the LOFZ (e.g. Lonquimay and Yate; Figure 1; Cembrano and Lara, 2009).

Primary melts in the SVZ are generated by dehydration of the subducted Nazca Plate and consequent partial melting of the lithospheric mantle wedge (Stern, 2004; Cembrano and Lara, 2009). Along-arc variations in the isotopic compositions of SVZ volcanic rocks indicate varying degrees of contribution from different processes in the production of these arc magmas (Cembrano and Lara, 2009). The signature of SVZ magmas can be altered by crustal assimilation (Hildreth and Moorbath, 1988), interaction with the continental lithosphere (Hickey-Vargas et al., 2002) and contamination of the magma source region due to subduction erosion (Stern, 1991). The relative contribution of the different processes will depend on a number of factors such as the composition and rheology of the continental crust, the crustal thickness, local and regional tectonic regimes (which will control magma ascent pathways), and the rate of subduction erosion (Cembrano and Lara, 2009).

Tholeiitic, high Al-basalts and basaltic andesites are the dominant products erupted from both stratovolcanoes and minor eruptive centres in the central and southern SVZ (south of 37° S; Hickey-Vargas et al., 1989; López-Escobar et al., 1995; Stern, 2004; Stern et al., 2007), while andesites, dacites and rhyolites are uncommon (Lara et al., 2006). The basalts of the central SVZ typically have lower than expected concentrations of MgO, Ni and Cr than basalts derived from primary mantle melts, which has been suggested to be due to deep fractional crystallisation (López-Escobar et al., 1995).

Regional tectonics control the alignment of volcanic chains in the SVZ, and the composition of erupted products. NE-striking alignments usually consist of basaltic and basaltic andesite stratovolcanoes and minor eruptive centres, while stratovolcanoes of a range of compositions are found in NW-striking alignments (López-Escobar et al., 1995; Cembrano and Lara, 2009). In general, NW-trending domains are more compressive, undergoing shortening and strike-slip deformation, resulting in longer magma residence time within the crust, allowing greater differentiation of eruptive products (López-Escobar et al., 1995; Cembrano and Lara, 2009).

2.2. *The Quetrupillán Volcanic Complex*

The Quetrupillán Volcanic Complex (Complejo Volcánico Quetrupillán), henceforth shortened to Quetrupillán, lies in the SVZ, at 39°30’ S, 71°43’ W. During the Holocene, activity at Quetrupillán has occurred from the summit of the stratocone and from at least sixteen vents around the flanks of the volcano (Figure 2), of which twelve form a volcanic field on the southern flank. The presence of icefields during the Holocene has resulted in extensive scouring of the stratocone, removing volcanic products erupted from the summit and covering the upper flanks with glacial till (Simmons et al., 2020).

The sixteen flank vents display a range of features: some have constructed scoria cones, some have excavated craters, some have built tuff rings, and some have neither excavated a crater nor constructed any feature around the vent. Most vents have also effused lava flows, ranging in size from less than 1×10^6 m^3 to over 60×10^6 m^3, though three vents have not produced any associated lava flow (Simmons et al., 2020). The variation in vent features and morphology implies that a variety of eruption styles occurred around the flanks of Quetrupillán during the Holocene. Scoria cones were built by conventional Strombolian activity, with scoria and volcanic bombs formed by magma fragmentation following ballistic trajectories (Valentine and Gregg, 2008; Valentine and Connor, 2015). Excavated craters formed when rising magma encountered groundwater and resulted in explosive phreatic eruptions, with tuff rings constructed around some craters when sufficient water enabled phreatomagmatic eruptions (Wohletz and Sheridan, 1983; Lorenz, 1986).

No detailed geological map of Quetrupillán has been published, and although uneroded Holocene vents and lavas are obvious in the field, no detailed field-based study has been published on either the pre-Holocene volcanic formations or on the structural evolution of the volcanic complex. Reconnaissance-level mapping led to the suggestion that an 8 km diameter caldera may exist (Pavez, 1997), but this has never been confirmed by detailed field observations and evidence has not been evaluated in peer-reviewed literature. No conclusive evidence confirming the presence of a caldera at Quetrupillán was found during this study.

Most (~96.7%) lava erupted from flank vents during the Holocene is trachytic in composition, with only minor trachyandesite and basaltic andesite lavas erupted (Simmons et al., 2020). The flank lava flows are predominantly composed of blocky lavas consisting of angular blocks of black, glassy trachyte lava. Where sampled, the composition of cone material is the same as the composition of any corresponding lava flow.

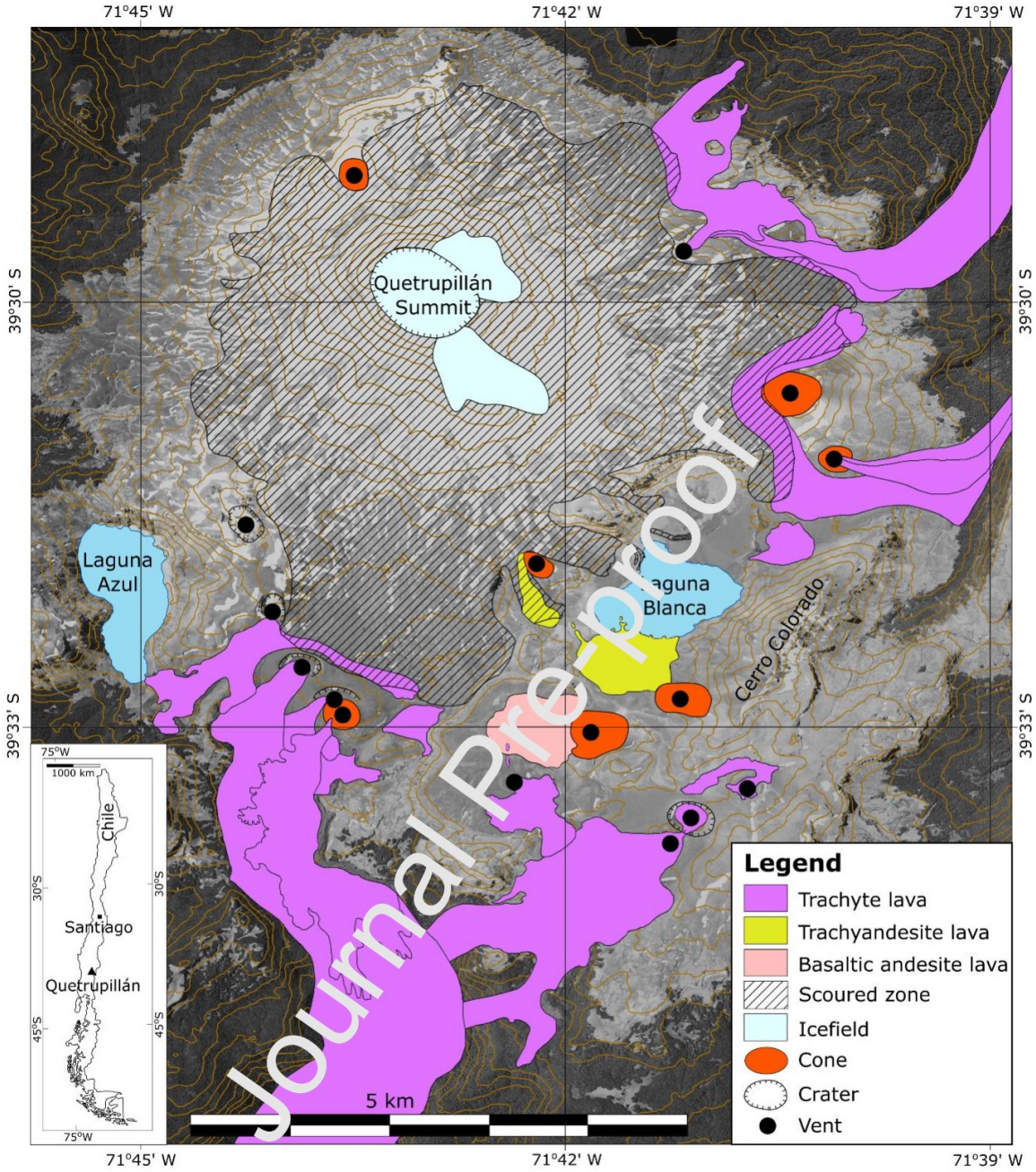

Figure 2: Map of the Holocene geology of Quetrupillán from the satellite flank vents (modified from Simmons et al., 2020). The glacially scoured zone (indicated by the hatched area) prevents mapping of Holocene products erupted from the summit region. The aerial photo background image is from the Servicio Aerofotogramétrico (SAF), Chile, and 50 m interval contours were obtained from a digital elevation model downloaded from earthexplorer.usgs.gov (downloaded 21/10/2016). The inset shows the location of Quetrupillán in Chile.

3. Methods

3.1. Sampling

Two field seasons were conducted at Quetrupillán, in February 2017 and January 2018, to map Holocene eruptive products and features, and to collect samples from lava deposits and pyroclastic sequences (see supplementary material for sample locations). Samples were collected from each Holocene lava flow produced by vents on the lower flanks of the volcano, and a selection of Holocene lavas erupted from the summit of the stratocone was also sampled. Pleistocene lavas were sampled by one of the authors (McGarvie) during prior field trips.

3.2. Geochemical analysis

Whole rock compositions of 66 Holocene and Pleistocene lavas and pyroclastic samples were analysed using a Panalytical PW2404 wavelength-dispersive sequential X-ray fluorescence (XRF) instrument, hosted at the University of Edinburgh (www.ed.ac.uk/geosciences/facilities/xrayfluorescence/xrf). Powdered samples were prepared as fused glass discs for major element analyses and pressed powder pellets for trace element analyses. Powders were heated at 1100°C for 20 minutes and the loss on ignition (LOI) of volatiles was recorded, tephra samples having first been heated overnight at 450°C to burn off any organic matter.

Rare earth element concentrations were measured in 14 selected samples (a sample from all except two flank vents) by inductively-coupled plasma mass spectrometry (ICP-MS). The analytical procedure is detailed in Olive et al. (2001), whereby dissolution of 0.1 g of sample powder was achieved by three-acid digestion (HF, HNO_3, HCl), followed by $HClO_4$ digestion to avoid the formation of insoluble fluorite and to ensure dissolution of spinel phases. Analyses were performed on the Agilent 7500ce ICP-MS instrument at the Scottish Universities Environmental Research Centre (SUERC; www.gla.ac.uk/research/az/suerc/researchthemes/isotopegeoscience/icp-ms-oes/), using the USGS BCR2 standard (Wilson, 1997) as a quality check.

Polished thin sections of 26 samples of lavas were cut, and these were studied under a petrological microscope. A subset of eighteen thin sections were analysed using the CAMECA SX100 electron microprobe at the University of Edinburgh (www.ed.ac.uk/geosciences/facilities/electron/instrumentspec) to determine mineral chemistry and glass compositions. Mineral phases were analysed using the following beam conditions: pyroxene with 2 µm beam diameter, 4 nA beam current and 15 kV accelerating voltage; plagioclase and olivine with initial conditions of 2 µm beam diameter, 4 nA beam current and 15 kV accelerating voltage, followed by 2 µm beam diameter, 100 nA beam current and 15 kV accelerating voltage; groundmass glass and melt inclusions were analysed with initial conditions of 5 µm beam diameter, 1 nA beam current and 15 kV accelerating voltage followed by 5 µm beam diameter, 80 nA beam current and 15 kV accelerating voltage. If measured, Na was analysed first to minimise its diffusion.

3.3. Geothermobarometry

Results from electron microprobe analysis (EMPA) of melt inclusions within clinopyroxene phenocryst hosts were used to estimate pressures and temperatures of crystallisation of Quetrupillán magmas. As the composition of the melt inclusion may continue to evolve due to post-entrapment fractionation, a correction for this was applied. Several post-entrapment corrections have been devised for the composition of melt inclusions hosted in olivine (e.g. Putirka, 2008; Danyushevsky and Plechov, 2011), based on the partition coefficient K_D $(Fe^{2+} – Mg)^{ol\text{-}liq}$ = 0.3 (Roeder and Emslie, 1970). This procedure involves adding the composition of the host olivine to the composition of the melt inclusion in 0.01% increments, until equilibrium is achieved. We adopted this approach to correct the composition of melt inclusions hosted in clinopyroxene, but with the following corrections: the partition coefficient is assumed to be K_D $(Fe^{2+} – Mg)^{cpx\text{-}liq}$ = 0.23 (Sisson and Grove, 1993); the speciation of iron in the clinopyroxene is calculated based on the charge balance in the mineral chemistry, following Papike et al. (1974) and Cameron and Papike (1981); the speciation of iron in the melt is calculated assuming the NNO buffer typical of arc products (Toplis and Carroll, 1995) and the calibration of Cortés et al. (2006).

Pressures were calculated using the clinopyroxene geobarometer of Nimis (1999a), computed using the CpxBar Excel spreadsheet (Nimis, 1999b), and temperatures were calculated from the clinopyroxene-liquid geothermometers presented as Equations 33 and 34 in Putirka (2008). Temperatures were calculated from Equation 33, unless the concentrations of Al_2O_3 and Na_2O in the clinopyroxene host were such that the jadeite component yields negative values, in which case temperatures were calculated from Equation 34. Both geothermometers (Equations 33 and 34) estimate temperatures with uncertainties of ± 45 °C (Putirka, 2008) and estimated pressures have uncertainties of ± 2 kbar (Nimis, 1999a). As the geothermometer requires an input of pressure and the geobarometer requires an input of temperature, these equations were solved iteratively until convergence of the results.

3.4. Structural analysis

The geometry of features and structures on Quetrupillán was measured from satellite imagery, downloaded from Google Earth and imported into Fiji (Schindelin et al., 2012). Visible features that were used in analysis include fissures, dykes, possible fault scarps, and orientation of asymmetric cones, as well as lineaments defined by topography and geomorphology. Many of these features were identified only from satellite imagery based on their aerial appearance, and so lack robust field evidence to support their identification. Holocene fissures were mapped in the field during this study, while Pleistocene fissures were mapped during previous fieldwork (McGarvie et al., 2014).

Fault scarps were not examined in the field, and so field observations of features to confirm the identification of faults (e.g. slickensides, brecciation along fault planes etc.) are unavailable, as are data such as fault offsets and the direction of fault motion. The identification of possible faults is therefore an assumption. The orientation of each lineament was measured and converted from a mathematical angle to a geological strike (from North at 000°) using the Fiji plugin Strike_Results.ijm (Cortés, 2019). Lineament orientations were imported into Stereonet (Allmendinger et al., 2013; Cardozo and Allmendinger, 2013) to generate rose diagrams.

4. Results

4.1. Geochemistry, petrography and mineral chemistry

Holocene lavas erupted from the summit of the stratocone range in composition from basalt to trachyte (52-64 wt.% SiO_2, 3.0-4.5 wt.% Na_2O, 1.0-3.2 wt.% K_2O), while Holocene lavas erupted from the flank vents range in composition from basaltic andesite to trachyte (55-65 wt.% SiO_2, 3.2-5.0 wt.% Na_2O, 1.5-3.1 wt.% K_2O; Figure 3; Table 1 and in supplementary material). This is a narrower compositional range than the whole rock compositions of the sampled Pleistocene lavas, which span from basalt to rhyolite (50-69 wt.% SiO_2, 2.9-5.6 wt.% Na_2O, 0.9-3.6 wt.% K_2O; Figure 3; see supplementary material). Most Holocene lavas are trachytic (62-65 wt.% SiO_2, 4.4-5.0 wt.% Na_2O, 2.7-3.2 wt.% K_2O). Twelve of the flank vents produced trachytic products, representing ~96.7% of the volume of Holocene lava erupted from flank vents (Simmons et al., 2020). Note that the "T" field on the Total Alkali Silica plot (Figure 3) includes both trachytes and trachydacites, but following the criteria in Le Maitre et al. (2002) for distinguishing between them, the Quetrupillán rocks in the "T" field are all trachytes.

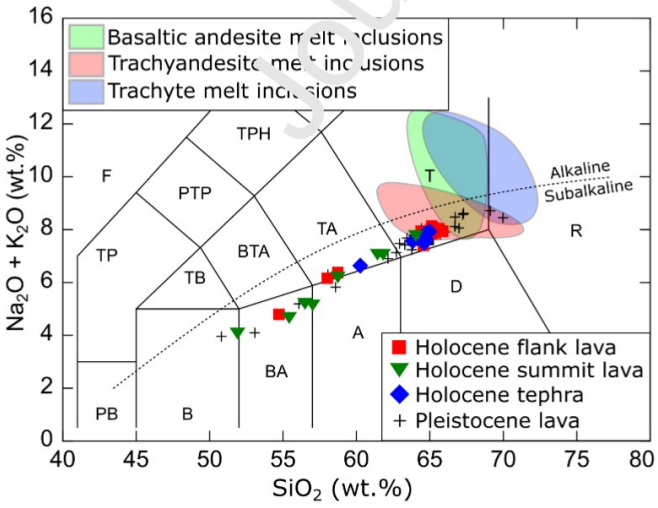

Figure 3: Total alkali silica (TAS) plot with whole rock compositions of Holocene flank lavas (red squares), Holocene summit lavas (green triangles), Holocene tephra deposits (blue diamonds) and

Pleistocene lavas (black crosses). Coloured regions indicate the composition of melt inclusions hosted in clinopyroxene crystals in lavas of different composition (green – basaltic andesite; red – trachyandesite; blue – trachyte). Classification is according to Le Maitre et al. (2002) and the dashed line represents the alkaline-subalkaline boundary proposed by Irvine and Baragar (1971).

Trachyte lavas are porphyritic (Figure 4A and B), containing 5-15% phenocrysts and glomerocrysts (normalised to vesicle-free). Plagioclase is the most abundant mineral phase, representing 50-70% of the phenocrysts, and has compositions from Andesine to Labradorite (An_{36-61}; Figure 5A; Table 2). One population of plagioclases have partially resorbed cores, surrounded by a zone of more calcic composition, before a return to the original composition at the phenocryst rim (Figure 6A and B).

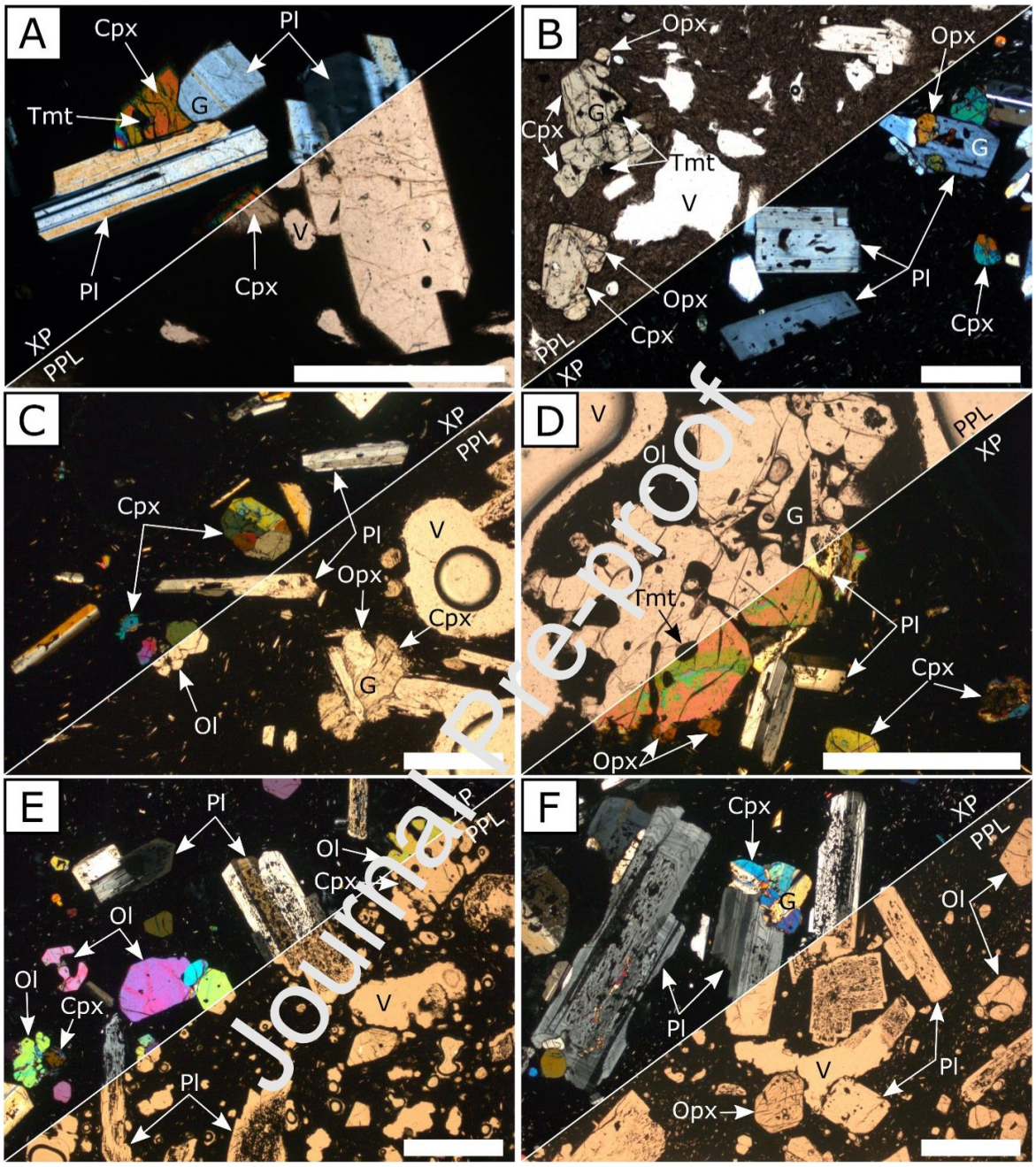

Figure 4: Thin section images of lavas from flank vents at Quetrupillán, of trachyte (A and B), trachyandesite (C and D) and basaltic andesite (E and F) composition. Pl – plagioclase, Cpx – clinopyroxene, Opx – orthopyroxene, Ol – olivine, Tmt – titanomagnetite, V – vesicle, G – glomerocryst. Scale bar in each image is 1 mm. Images show thin sections under plane polarised light (PPL) and under crossed polars (XP). Modified from Simmons et al. (2020).

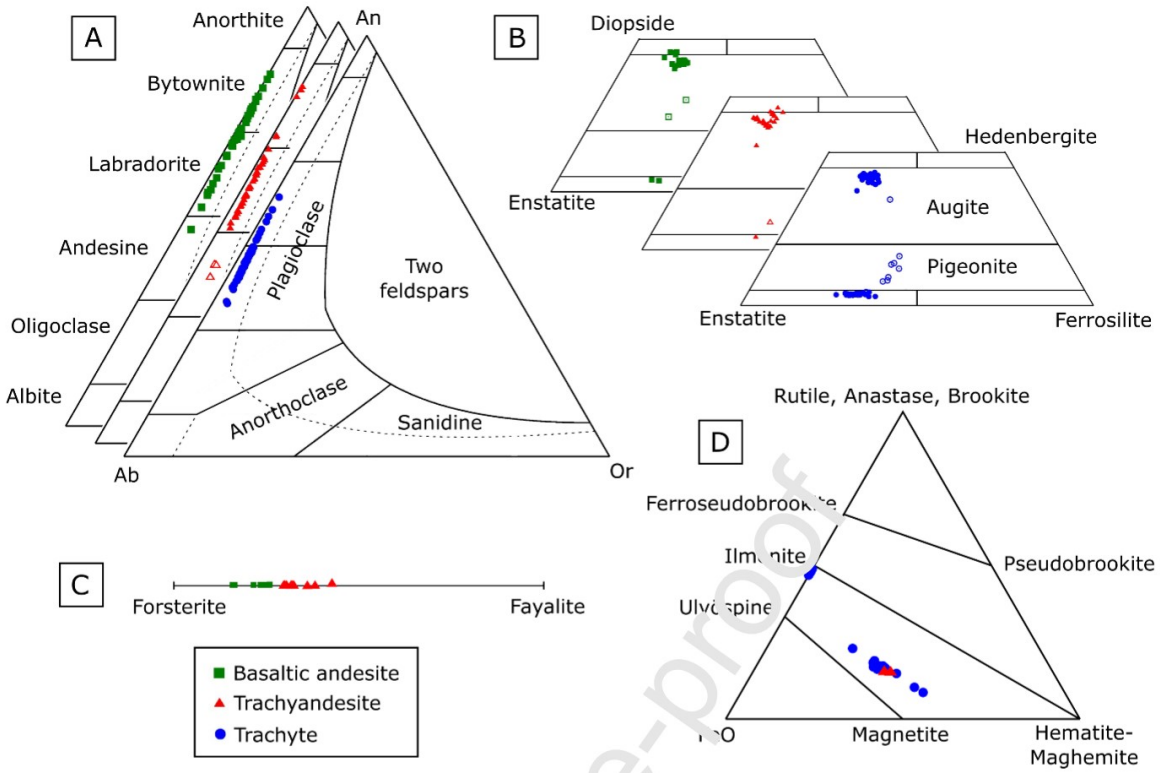

Figure 5: Mineral chemistry of plagioclase (A), pyroxene (B), olivine (C) and oxide (D) phenocrysts are arranged by whole rock composition: basaltic andesite – green squares, trachyandesite – red triangles, trachyte – blue circles. Open symbols represent groundmass microlites.

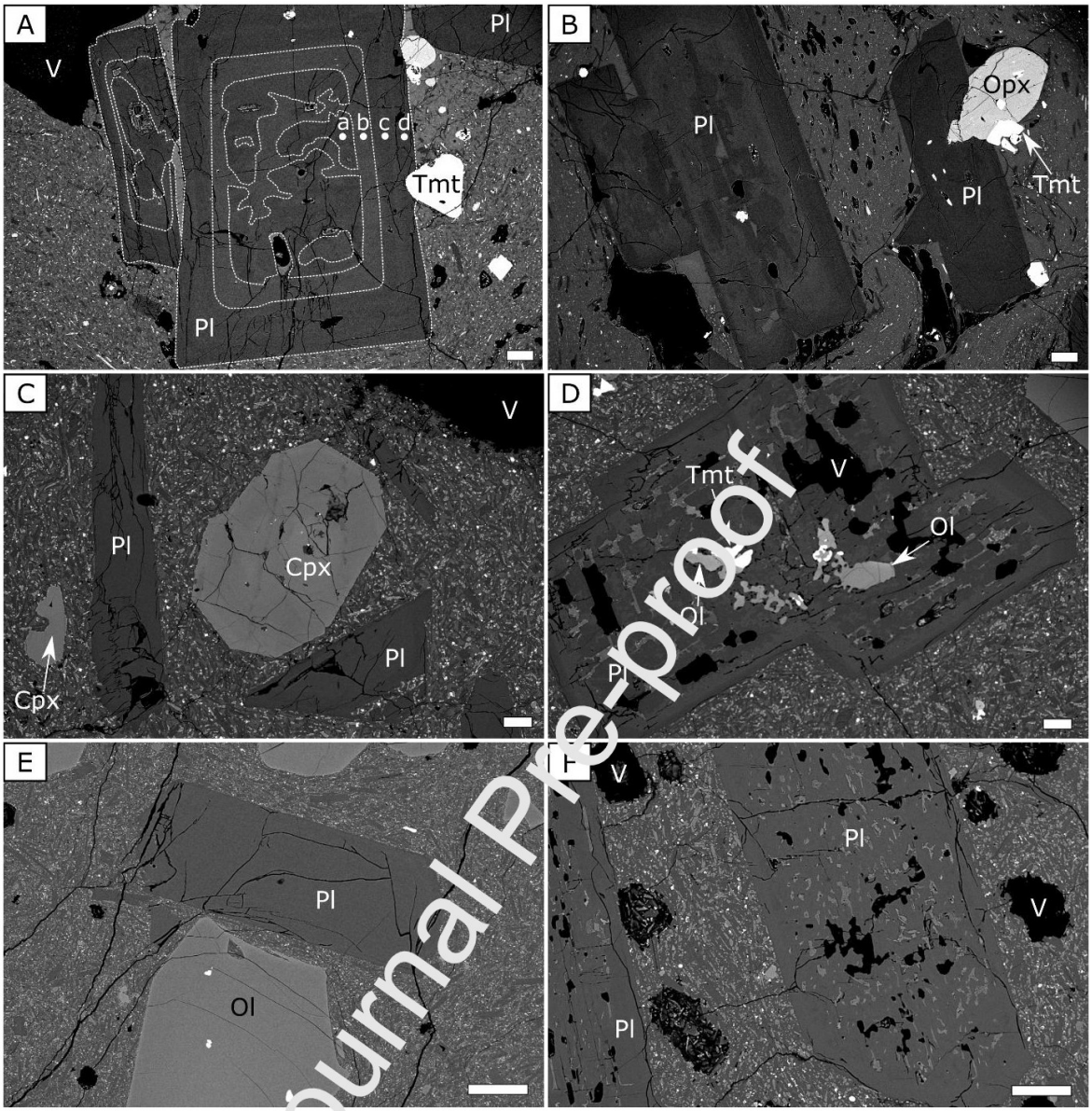

Figure 6: BSE images of different populations of plagioclase phenocrysts. A) A plagioclase phenocryst in trachyte lava with a partially resorbed core (a – An_{47}), surrounded by a more calcic zone (b – An_{54}), before a return to the original composition for the rim (c – An_{46}; d – An_{46}); B) plagioclase phenocrysts in trachyte lava, with partially resorbed core (left) and pristine texture (right); C) pristine plagioclase phenocrysts in trachyandesite lava; D) sieve-textured plagioclase phenocryst in trachyandesite lava; E) pristine plagioclase phenocryst in basaltic andesite; F) sieve-textured plagioclase phenocrysts in basaltic andesite. Pl – plagioclase, Cpx – clinopyroxene, Opx – orthopyroxene, Ol – olivine, Tmt – titanomagnetite, V – vesicle. Scale bar in each image is 100 µm.

Ortho- and clinopyroxene phenocrysts comprise 15-40% of the phenocryst population in trachyte lavas (Augite; Mg# 67-77, and Enstatite; Mg# 61-73; Figure 5B). Trachyte lavas also contain

Titanomagnetite and Ilmenite, which form a minor constituent of the phenocryst assemblage (2-10%; Figure 5D).

Trachyte lavas have glassy groundmass with a composition of trachyte to rhyolite (63-72 wt.% SiO_2, 4.0-6.9 wt.% Na_2O, 1.8-5.7 wt.% K_2O), containing microlites of the same mineral phases plus Pigeonite, and minor Apatite as an accessory phase. Melt inclusions within ortho- and clinopyroxene hosts have similar compositions (66-72 wt.% SiO_2, 4.0-8.6 wt.% Na_2O, 3.0-5.9 wt.% K_2O) though some have anomalously high alkali contents (up to 12 wt.% $Na_2O + K_2O$; Figure 3).

Two Holocene flank vents produced trachyandesite lava flows, representing ~1.8% of the volume of Holocene lava erupted from flank vents (Simmons et al., 2020). Trachyandesite lavas are also porphyritic (Figure 4C and D) and have a higher abundance of phenocrysts and glomerocrysts than trachyte lavas (~30%). Plagioclase is the dominant mineral phase (~50%), with compositions varying from Labradorite to Bytownite (An_{51-84}; Figure 5A). There are two distinct plagioclase populations, one of pristine phenocrysts and one showing sieve textures (Figure 6C and D). Ortho- and clinopyroxene phenocrysts (~23%) occur as Augite to Diopside (Mg# 67-82) and rare Enstatite (Mg# ~68; Figure 5B). Trachyandesite lavas also contain ~15% olivine (Fo_{57-70}; Figure 5C), often with resorbed rims, and ~2% Titanomagnetite (Figure 5D). The groundmass of trachyandesite lavas is fully crystalline, composed of the same mineral phases, though plagioclase groundmass crystals are more sodic with a composition of Andesine (An_{39-42}; Figure 5A). Melt inclusions in clinopyroxene hosts have trachytic to rhyolitic glass compositions (62-70 wt.% SiO_2, 4.4-6.0 wt.% Na_2O, 2.2-5.4 wt.% K_2O; Figure 3).

Only one Holocene flank vent produced a basaltic andesite lava flow, accounting for ~1.5% of the volume of Holocene lava erupted from flank vents (Simmons et al., 2020). The basaltic andesite lava is porphyritic, with ~37% phenocrysts (Figure 4E and F). Plagioclase is still the most abundant mineral phase, comprising ~40% of the phenocrysts, with compositions ranging from Andesine to Bytownite (An_{47-84}; Figure 5A). Phenocrysts are up to 2 mm, and most have highly sieve-textured interiors though some have pristine textures (Figure 6E and F). The secondary phenocryst phase in basaltic andesite lava is olivine (Fo_{74-84}; Figure 5C) which accounts for ~35% of the phenocrysts. Some olivines have resorbed rims while others display pristine crystal morphologies (Figure 4E). Ortho- and clinopyroxene phenocrysts comprise ~23% of phenocrysts in the basaltic andesite lava and consist of Augite to Diopside (Mg# 69-81) and rare Enstatite (Mg# 69-72; Figure 5B). There is also minor (~2%) Cr-spinel as an accessory phase. Melt inclusions in clinopyroxene hosts have compositions of trachyte (64-69 wt.% SiO_2, 3.8-6.5 wt.% Na_2O, 2.2-6.4 wt.% K_2O; Figure 3).

The rare earth elements (REE) diagram (Figure 7A), normalised to chondrite (Sun and McDonough, 1989), discriminates between the three different lava compositions. Trachyte lavas have the greatest values of rock/chondrite for each element, while the basaltic andesite lava has the lowest values. Lavas of all three composition have a gentle slope (La/Yb ~7-9) and display a small negative Eu anomaly. The spider diagram (Figure 7B; Pearce, 1983), normalised to normal mid ocean ridge basalt (N-MORB) according to Sun and McDonough (1989), also distinguishes between the three lava compositions. All lavas have a small negative Nb anomaly and are enriched in high field strength elements (HFSE) compared to N-MORB. Trace element ratio plots (Figure 7C-F) also distinguish between samples of different whole rock composition. Plotting Rb against Cr (Figure 7F) shows a steepening curve from basaltic andesite to trachyandesite to trachyte.

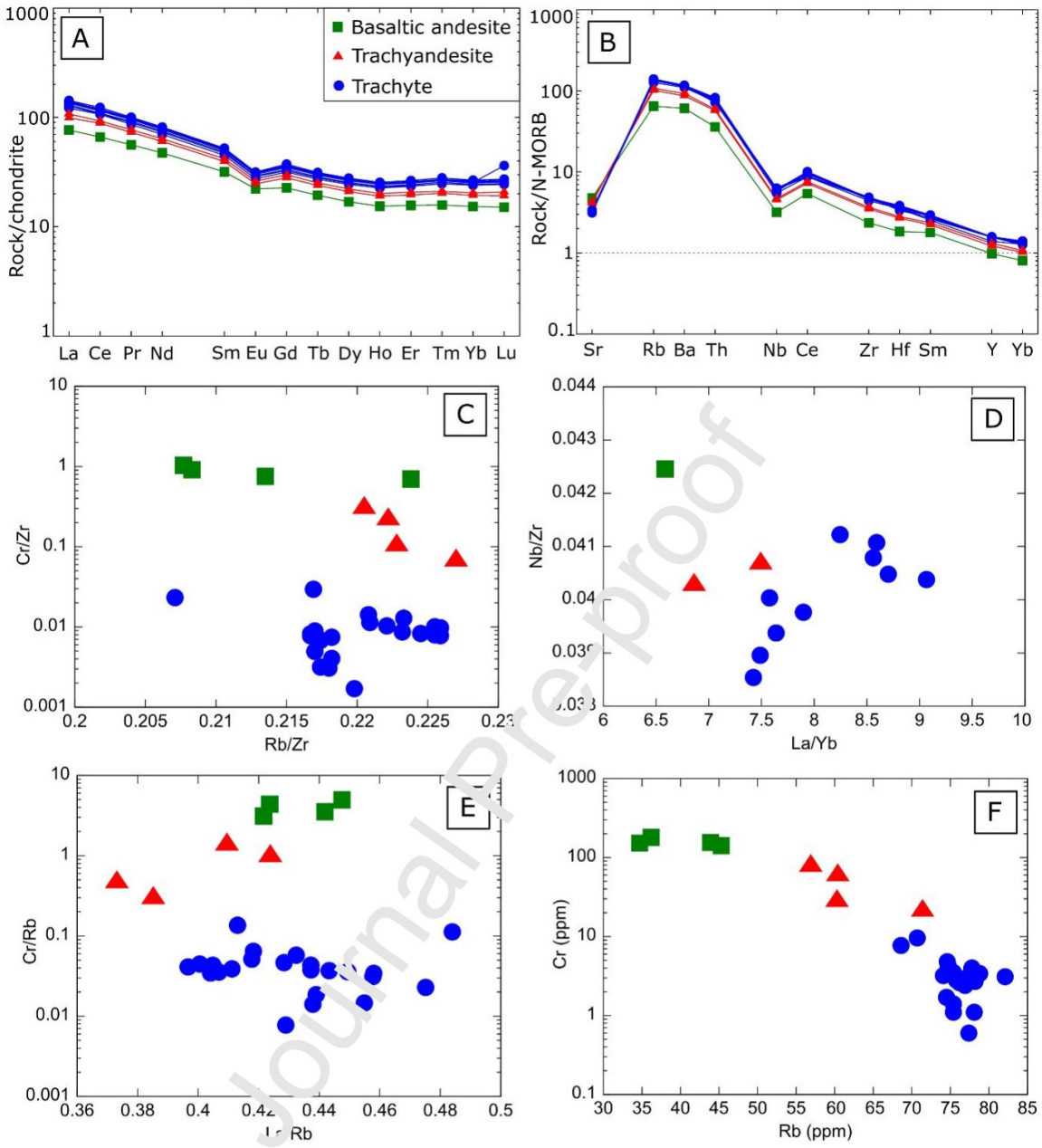

Figure 7: Rare earth and trace element plots. A) REE diagram, normalised to chondrite (Sun and McDonough, 1989); B) spider diagram (Pearce, 1983), normalised using N-MORB (Sun and McDonough, 1989), with large ion lithophile elements (LILE) to the left and high field strength elements (HFSE) to the right; C) Rb/Zr vs Cr/Zr; D) La/Yb vs Nb/Zr; E) La/Rb vs Cr/Rb and F) Rb vs Cr. Samples symbols are according to whole rock composition: basaltic andesite – green squares, trachyandesite – red triangles, trachyte – blue circles.

4.2. Geothermobarometry

Seventeen pairs of melt inclusions within clinopyroxene hosts were used to estimate temperatures and pressures of crystallisation in trachyte, trachyandesite and basaltic andesite magmas (Figure 8;

see supplementary material). Calculated temperatures range from 913-1020 ± 45 °C for trachyte lavas, 997-1001 ± 45 °C for trachyandesite lava and 941-1022 ± 45 °C for basaltic andesite lavas. Pressures range from 1.2-6.9 ± 2 kbar for trachyte lavas, 3.2-4.0 ± 2 kbar for trachyandesite lava and 3.5-6.1 ± 2 kbar for basaltic andesite lavas. Assuming a crustal density of 2800 kg/m^3 (Weidmann et al., 2013), these pressures correspond to depths of ~4-25 km for trachyte lavas, ~12-15 km for trachyandesite lava and ~13-22 km for basaltic andesite lava, with most calculated depths between 7 and 19 km (Figure 8). It should be noted that no independent determination of crystallisation pressures and temperatures was achieved, as these two variables were solved iteratively.

Unlike the clinopyroxene-liquid geothermometer of Putirka (2008), which depends upon the composition of the melt in equilibrium with the clinopyroxene, the geobarometer of Nimis (1999a) depends upon the clinopyroxene composition and the nature of the magma (subalkaline in the case of Quetrupillán; Figure 3), to estimate pressures of crystallisation. As the equilibrium melt is not necessary for estimation of pressure, the geobarometer was also used to estimate the pressures of crystallisation for 40 clinopyroxene phenocrysts in trachyte lavas that do not contain melt inclusions (i.e. do not have a proxy of the equilibrium melt), in order to increase the dataset. EMPA analyses were made in the core of clinopyroxene phenocrysts, and a temperature of 968 °C was used for all pressure calculations, as this is the average of temperatures calculated iteratively from clinopyroxene-melt pairs. This generated pressure estimates of 2.3-4.8 ± 2 kbar, corresponding to depths of ~8-18 km (Figure 8), within the range of pressures estimated from clinopyroxene-melt pairs.

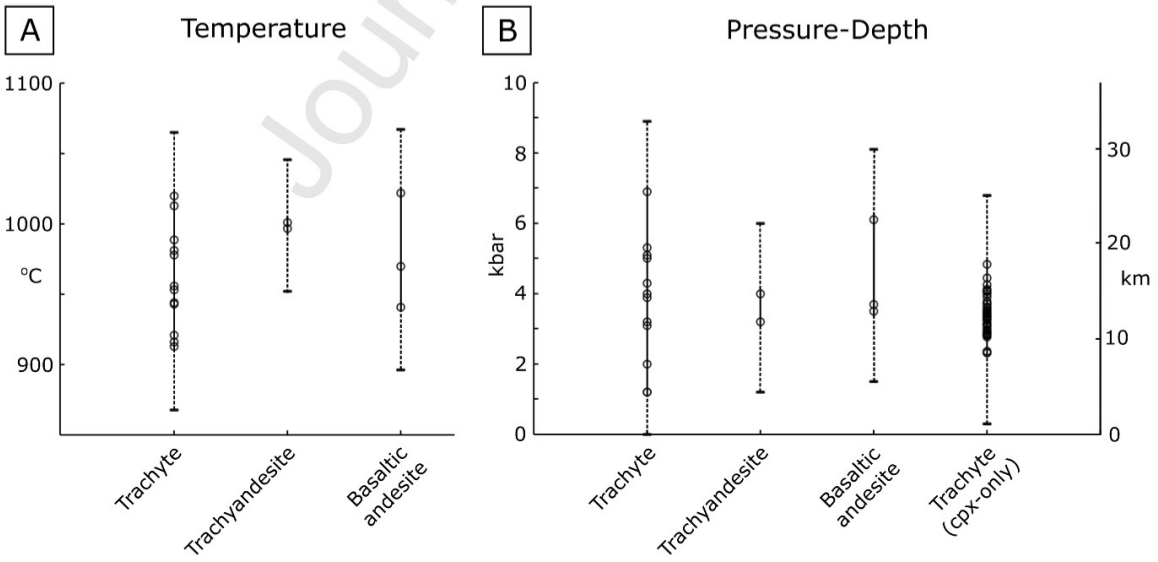

Figure 8: Estimated temperatures (A) and pressures (B) from clinopyroxene-melt pairs in trachyte, trachyandesite and basaltic andesite lavas. Depths (B) are calculated assuming a crustal density of

2800 kg/m^3 (Weidmann et al., 2013). The "Trachyte (cpx-only)" datapoints (in B) are pressures and depths estimated using clinopyroxenes in trachyte lavas that did not contain melt inclusions, assuming a temperature of 968 °C. Solid lines connect estimated values (circles) and dashed lines represent the uncertainties of 45 °C (Putirka, 2008) and 2 kbar (Nimis, 1999a).

4.3. Structural analysis

Forty-four lineaments (e.g. fissures, dykes, possible fault scarps) were identified and measured from satellite imagery of Quetrupillán, and their orientations were plotted in rose diagrams (Figure 9). When considering the whole area around Quetrupillán, lineaments have a primary preferential orientation of NW-SE and a secondary orientation of NNE-SSW (Figure 9B). No lineaments are oriented W-E, and almost none are oriented N-S. Most observed lineaments are oriented tangentially to the summit, rather than radially to it. However, as the scoured zone is covered with glacial till, there may be radially-oriented lineaments around the stratocone summit that have not been observed.

To enable comparison of lineaments across different zones of Quetrupillán, the volcano was divided into quadrants, centred on the southern rim of the summit crater (due to the asymmetric shape of the main edifice this is more central than the middle of the crater; Figure 9A) and aligned N-S as this is the approximate orientation of the LOFZ . This division results in clear differences in lineament orientation across different flanks of the volcano (Figure 9C). In the northeast and southwest quadrants, lineaments are mainly oriented NW-SE, while in the southeast quadrant, lineaments are mostly perpendicular to this orientation, aligned NE-SW. In the northwest quadrant, lineaments mainly follow two preferred orientations at NW-SE and NNE-SSW. Differences in lineament orientation across flanks are also observed when the flanks are divided into North, South, East and West (Figure 9D). Lineaments in the western and southern quadrants are mainly oriented NW-SE. In the eastern quadrant lineaments have two perpendicular orientations at NE-SW and NW-SE. Lineaments in the northern quadrant show no preferential orientation.

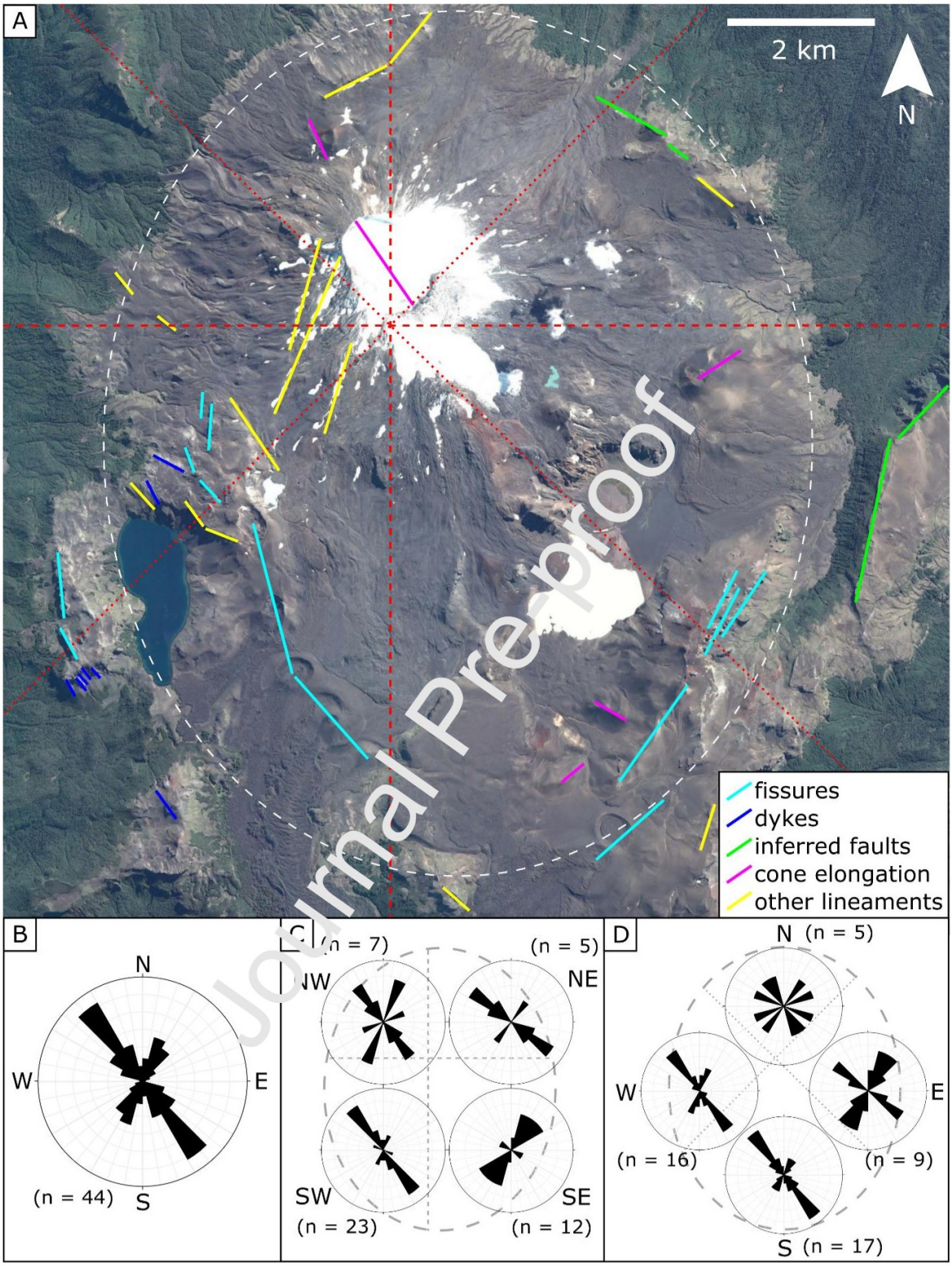

Figure 9: A) Identified structural lineaments on the flanks of Quetrupillán (light blue – Holocene and possible Pleistocene fissures; dark blue – dykes; green – inferred faults; pink – cone elongation; yellow – other lineaments defined by topography and geomorphology) with the flanks divided into segments (red dotted lines divide N-E-S-W quadrants; red dashed lines divide NW-NE-SE-SW

quadrants; white dashed oval represents the volcano outline used in C and D); B) rose diagram of all 44 lineaments; C) rose diagrams of flanks divided into NW-NE-SE-SW quadrants; D) rose diagrams of flanks divided into N-E-S-W quadrants. Google Earth image downloaded 24/02/2020.

5. Discussion

5.1. Petrology and geochemistry

Clinopyroxene phenocrysts in basaltic andesite and trachyandesite lavas, erupted from the flanks and summit of Quetrupillán, contain melt inclusions of trachytic composition (Figure 3). They also show an overlap in ranges of pressures and temperatures of crystallisation calculated by geothermobarometry (Figure 8). The composition of these melt inclusions, and the pressure and temperature results, strongly suggest that these clinopyroxene phenocrysts crystallised in a trachytic melt and they are xenocrysts in the basaltic andesite and trachyandesite lavas.

The basaltic andesite and trachyandesite lavas also contain uncommon phenocrysts of orthopyroxene which exist alongside the abundant phenocrysts of olivine (Figures 4 and 5). As olivine and orthopyroxene should not co-exist in equilibrium within a melt (e.g. Carmichael et al., 1970), the presence of these phases strongly suggests that magma mixing has resulted in hybrid compositions. The high Forsterite content of olivines in the basaltic andesite lava (Fo_{74-84}) indicates that they have crystallised from a relatively primitive basaltic melt. In contrast, the orthopyroxene phenocrysts have crystallised in a more evolved melt. Like the clinopyroxenes with trachytic melt inclusions, the orthopyroxene phenocrysts are likely to be xenocrysts in the basaltic andesite and trachyandesite lavas. Olivine phenocrysts in the trachyandesite lavas have lower Forsterite contents (Fo_{57-70}), which suggests that olivine continued to crystallise in the hybrid trachyandesite melt after the mixing event.

In contrast to the basaltic andesite and trachyandesite lavas, the mineral assemblage in the Holocene trachytes appears to be in equilibrium with the whole rock composition. The trachyte lavas contain two pyroxene populations (opx and cpx) and plagioclase with compositions of Andesine to Labradorite (An_{36-61}), within trachytic to rhyolitic glass (Figures 3 and 5). This strongly suggests that the phenocryst assemblage in the trachyte lavas crystallised from the melt represented by the whole rock composition. However, variations in the composition of melt inclusions, groundmass glass and the plagioclase phase suggest a range of melt compositions from which the trachyte lavas have been derived. Within individual samples, melt inclusions in ortho- and clinopyroxenes have similar compositions to groundmass glasses, suggesting that trachyte lavas crystallised in equilibrium with the melt in which they formed. This crystallisation is calculated to have occurred over a wide range

of pressures (Figure 8), suggesting that crystallisation of clinopyroxene phenocrysts happened across a range of depths (~7-19 km) below the volcano.

5.2. Textural implications

Sieve-textured plagioclases are uncommon in Quetrupillán's trachyte lavas, but abundant in trachyandesite and basaltic andesite lavas, where many plagioclase phenocrysts have well defined sieve textures (Figures 4 and 6). The mineral chemistries of plagioclase phenocrysts appear to be in chemical equilibrium with their whole rock composition (An_{47-84} in the basaltic andesite, An_{51-84} in the trachyandesite and An_{36-61} in the trachyte), suggesting that the sieve textures are not the result of magma mixing leading to chemical disequilibrium. If sieve texture is not the consequence of chemical disequilibrium, it can be produced by increasing temperature or decreasing pressure (Nelson and Montana, 1992). As we have estimated a wide range of pressures for the magmatic system, we favour rapid decompression during magma ascent. Along these lines, the occurrence of zoned plagioclases could be interpreted as crystal growth happening in a heterogeneous melt or in a melt of changing compositions, or as a result of mixing events (e.g. Ginibre et al., 2002).

5.3. REE and trace elements

The REE profiles of trachyte, trachyandesite and basaltic andesite lavas (Figure 7A) all have a gentle slope and display a small negative Eu anomaly, suggesting fractionation of plagioclase in the mantle source (Rollinson, 1993), which is the dominant mineral phase in all Quetrupillán lavas. The relatively flat REE profile (La/Yb ~7-9; Figure 7D) suggests there has been little or no fractionation of garnet, following the extraction of the parental melt from the mantle source, as this would lead to a steeper REE profile (Rollinson, 1993). The absence of garnet fractionation in the generation of Quetrupillán melts suggests that the primary melts have been generated within the lithospheric mantle.

The spider diagram (Figure 7B) of Holocene lava samples from Quetrupillán shows enrichment of HFSEs compared to an uncontaminated melt derived from a N-MORB source. In comparison, the HFSEs in lavas erupted from Villarrica (Figure 10) do not show this enrichment compared to N-MORB (except in Ce) as values of rock/N-MORB plot at around 1. Data from Lanín and Sollipulli show a similar pattern (Figure 10; see supplementary material for data and references), but with variable levels of enrichment, spanning the range observed at Quetrupillán and Villarrica. Evolved products from Lanín and Sollipulli have HSFE ratios similar to those of Quetrupillán, while basalts from Lanín and Sollipulli have HFSE ratios similar to those of Villarrica.

This strongly suggests a common mantle source for these volcanoes (N-MORB), that undergoes variable amounts of contamination. Villarrica represents little or no enrichment, while at Quetrupillán, enrichment is higher. At Lanín and Sollipulli, enriched products are similar to

Quetrupillán lavas, while non-enriched products are similar to Villarrica lavas. We propose that this enrichment is likely from crustal assimilation, and that Villarrica and Quetrupillán represent end members of the extent of enrichment.

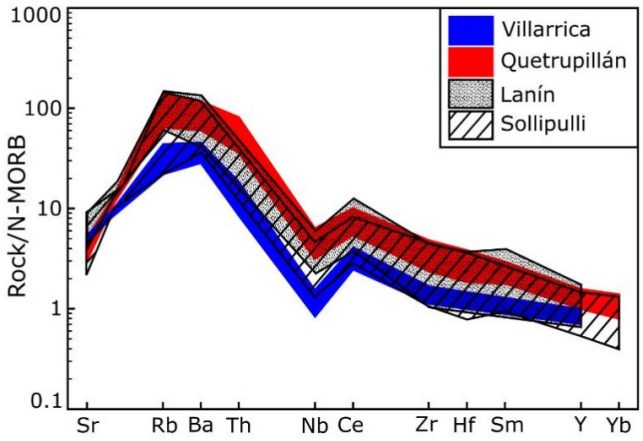

Figure 10: Spider diagram of lavas from Quetrupillán (red field: this study, Holocene samples only), Villarrica (blue field), Lanín (dotted field) and Sollipulli (hatched field). See supplementary material for data and references for Villarrica, Lanín and Sollipulli

Figures 7C to 7E show different combinations of compatible-incompatible (Cr/Zr, Cr/Rb) and incompatible-incompatible (La/Yb, Rb/Zr) ratios to test for a common source and provide insights on the fractionation process. The relatively small variation in incompatible-incompatible ratios clearly supports a common single source for these magmas, while the observed decreasing trend in compatible-incompatible ratios (e.g. Cr/Rb) supports a fractionation model as the main process for magma evolution. The trend in the plot of Rb vs Cr (Figure 7F) with a slight enrichment in Rb, compared with the expected evolution of Rb in a fractionation-only model, is compatible with the contamination hypothesis and longer crustal residence time during fractionation. As Cr-spinel occurs in basaltic andesite lavas, the early fractionation of this phase might have played an important role in Cr behaviour. Additionally, although chromium is incompatible in olivine (crystallising in a basalt or a basaltic andesite) it is compatible in clinopyroxene (Rollinson, 1993), suggesting a process with the initial fractionation of olivine in the basaltic andesite, followed by the fractionation of olivine + clinopyroxene.

5.4. Quetrupillán magma generation

In this region of the SVZ, basaltic melt is produced by dehydration of the subducted slab and the partial melting of a mantle source (Hildreth and Moorbath, 1988; Stern et al., 2007; Hickey-Vargas et al., 2016a). Deep fractionation of this melt will provide the source of magmas erupted in the region (Stern, 2004; Cembrano and Lara, 2009). Basalts are significant constituents of erupted products

from Villarrica and Lanín (Figure 11; Clavero and Moreno, 2004; Lara et al., 2004), and are minor products erupted by Quetrupillán (Figure 3). Basalts have also been erupted by eight minor eruptive centres (MECs) that are located 12-35 km north of Quetrupillán, including Huililco, Caburgua and San Jorge (McGee et al., 2017). The abundance of basalt produced by surrounding volcanoes suggests that the composition of the original source melt at Quetrupillán is likely to be basaltic.

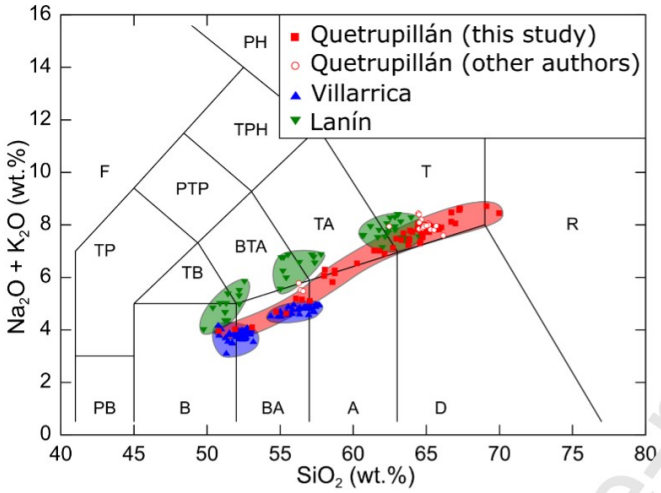

Figure 11: TAS plot of whole rock analyses of samples from Villarrica (blue triangles), Quetrupillán (red squares – this study; red open circles – other authors) and Lanín (green inverted triangles). Data and data sources are listed in the supplementary material.

Previous authors (Pavez, 1997; Brahm et al., 2018) have suggested that the basaltic to basaltic andesite MEC of Huililco, which lies 12 km northeast of Quetrupillán's summit, represents the parental melt of Quetrupillán. As a result, Huililco basalt has been used in modelling calculations to determine the generation of Quetrupillán magmas (Brahm et al., 2018). During fieldwork, we identified a Holocene basaltic lava flow on the flanks of Quetrupillán, assumed to have erupted from the summit region. This provides a parental melt composition that is definitely present in the magmatic plumbing system below Quetrupillán, rather than a composition erupted from Huililco, a different volcano, 12 km away from Quetrupillán's main edifice.

This Holocene basalt is porphyritic, with phenocrysts of plagioclase, olivine, clinopyroxene and an oxide phase in a highly crystalline groundmass of the same minerals. We modelled mixing of this basalt sample from Quetrupillán (Q67; Table 1) with a representative trachyte sample from Quetrupillán (Q3; Table 1) using the online tool Olive 2.1.1 (Cortés, 2016). Modelled major element concentrations match the major element concentrations of erupted Holocene basaltic andesite and trachyandesite lava samples (Figure 12).

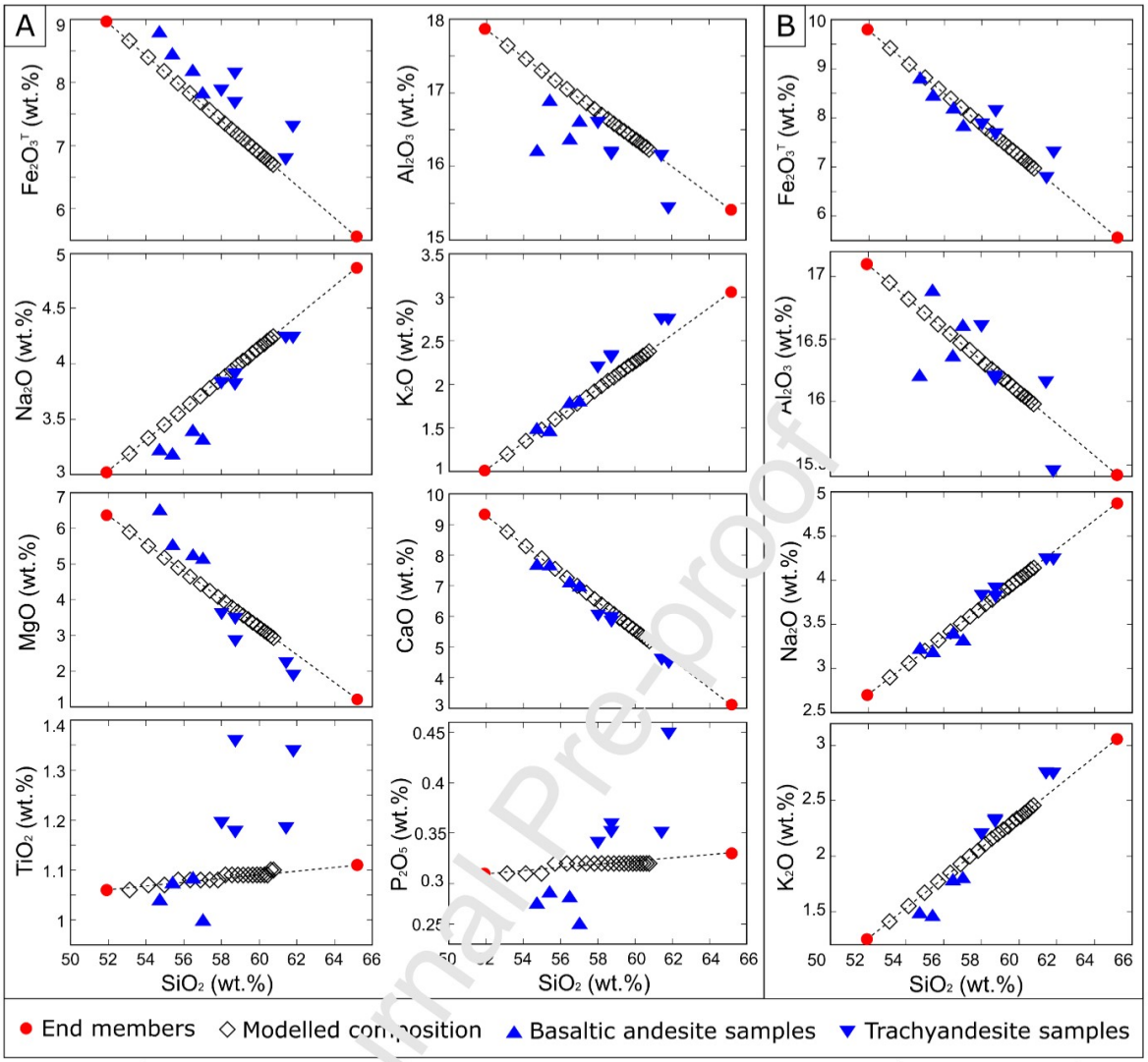

Figure 12: A) Harker diagrams showing modelled major element compositions (black diamonds) when mixing a basalt lava sample from Quetrupillán (Q67) with a trachyte lava sample (Q3; red circles). Basaltic andesite samples (blue triangles) and trachyandesite samples (inverted blue triangles) from Quetrupillán are also plotted. Some mixing ratios are labelled in the plot of SiO_2 vs Na_2O. B) Harker diagrams showing the same modelling, but with altered Fe_2O_3 (9.8 wt.%), Al_2O_3 (17.1 wt.%), Na_2O (2.7 wt.%) and K_2O (1.25 wt.%) in the basalt input.

Mixing 77% basalt and 23% trachyte (sample Q67 and Q3 respectively; Table 1) produces a basaltic andesite very similar to the basaltic andesite erupted from the flanks of Quetrupillán, and mixing 71% basalt with 29% trachyte produces a composition similar to basaltic andesite erupted from the summit of Quetrupillán. The two trachyandesite flank lava compositions are reproduced when mixing 56% and 48% basalt with 44% and 52% trachyte, respectively.

The modelled compositions generated when mixing Quetrupillán basalt and trachyte lavas are a close fit in the concentration of CaO, Na_2O, K_2O and MgO when compared to the basaltic andesite and trachyandesite lavas erupted from the flanks and summit of Quetrupillán. The modelled compositions underestimate the concentration of $Fe_2O_3^T$ in the basaltic andesite and trachyandesite samples and overestimate the concentration of Al_2O_3. Neither TiO_2 nor P_2O_5 are well modelled, due to their low concentrations in all Quetrupillán samples. TiO_2 is present in Ilmenite and Titanomagnetite, and P_2O_5 is present in Apatite, all accessory phases in Quetrupillán lavas that have not been considered in the presented modelling.

The basalt lava that erupted at Quetrupillán may have been altered from its original, parental composition, resulting in the observed variations between the modelled and erupted basaltic andesites and trachyandesites. By altering the composition of the basalt input in the modelled mixing, a closer fit to the basaltic andesite and trachyandesite samples can be achieved (Figure 12B). The concentration of $Fe_2O_3^T$ was increased from 8.97 wt.% to 9.8 wt.%, and the concentration of Al_2O_3 was decreased from 17.87 wt.% to 17.1 wt.%. Although the modelled compositions have a close fit for Na_2O and K_2O, Na_2O is overestimated for basaltic andesite samples and K_2O is underestimated for trachyandesite samples. To improve the fit of the modelled compositions, the concentration of Na_2O in the basaltic input was decreased from 3.02 wt.% to 2.7 wt.%, and the concentration of K_2O was increased from 1.01 wt.% to 1.25 wt.%, resulting in modelled compositions closer to those present in the basaltic andesite and trachyandesite samples of Quetrupillán.

The mixing of basalt and trachyte to produce the basaltic andesite and trachyandesite magmas is also supported by plotting major and trace element concentrations on an abacus diagram (Figure 13). The basaltic andesite and trachyandesite lavas from flank vents plot as near-vertical lines, indicating that they are very likely to be hybrid magmas formed by mixing the selected trachyte and basalt end member magmas (McGarvie et al., 1990). Mixing of ~80% basalt with ~20% trachyte can produce the basaltic andesite lava and mixing of ~35-45% basalt with ~55-65% trachyte can produce the trachyandesite lavas, consistent with the proportions found using just major elements (Figure 12). The mixing relationship is not perfect, as the basaltic andesite sample (Q50) is offset from a vertical line for Sr and Nb and the trachyandesite samples (Q8 and Q17) are slightly offset for SiO_2, CaO, Nd, and La. It should be noted that this diagram only produces near-vertical mixing lines when both end member magmas and the hybrids produced by mixing them occur in the same eruption. This does not occur at Quetrupillán, as magma mixing takes place at depth, and only the hybrid magma is erupted.

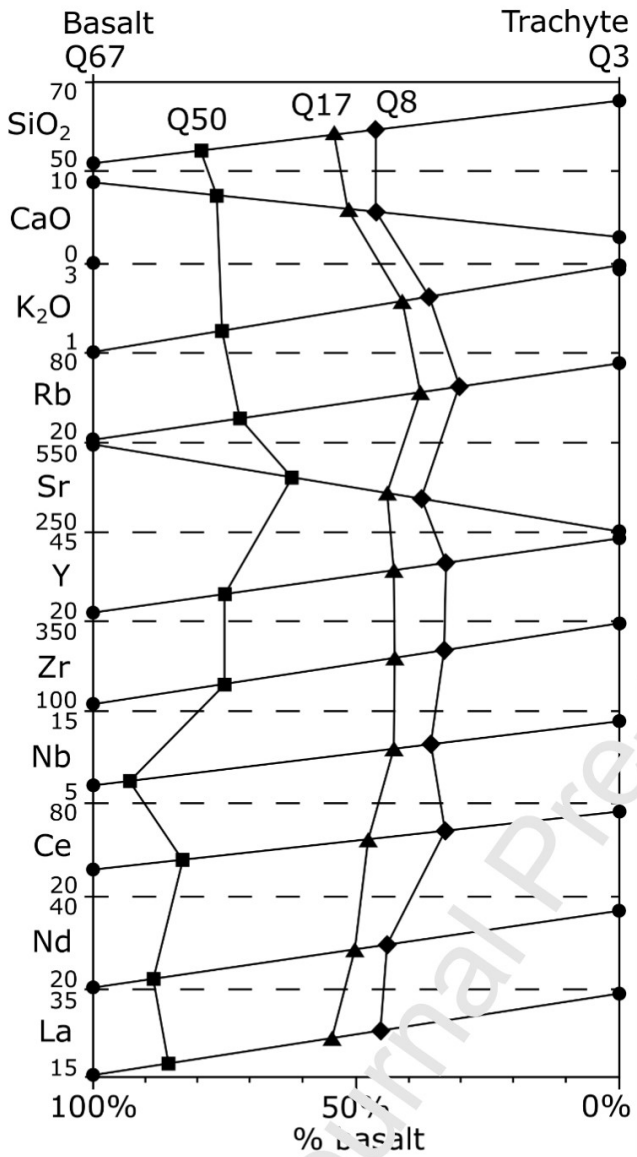

Figure 13: Abacus diagram illustrating mixing between a trachyte end member magma (Q3) and a basalt end member (Q67). The x-axis shows the proportion of the basalt end member magma, and the y-axis gives major element (oxide wt.%) and trace element (ppm) concentrations. On this diagram, hybrid compositions produced by mixing together the two selected end member magmas will produce straight vertical lines (McGarvie et al., 1990). The compositions of the basaltic andesite (Q50 – squares) and trachyandesite (Q8 – diamonds; Q17 – triangles) flank vent lavas are plotted.

Consequently, the precise composition of the two end member magmas is not known, although the abundance and restricted compositional range of Holocene trachyte lavas provides a good approximation of the likely trachyte end member. The strong similarity in the range of compositions that have been erupted during both the Pleistocene and Holocene (Figure 3) suggests a continuity in the generation of magmas produced beneath Quetrupillán through time.

The basalt sample used as the basaltic end member for mixing with trachyte has total mineral proportions (converted to weight percent) of 28% olivine, 20% clinopyroxene, 32% plagioclase and 20% oxide. Modelling batch fractionation of these mineral proportions (assuming the oxide phase is all Magnetite) from the basaltic andesite sample can reproduce the REE concentrations observed in the trachyandesite and trachyte samples from Quetrupillán (Figure 14). The trachyte REE profile is reproduced when F=0.7 and the trachyandesite REE profile is reproduced when F=0.4, though in both cases the concentrations of La and Ce are underestimated by the model. As fractionating the mineral assemblage equivalent to the basalt from the basaltic andesite is able to reproduce the trachyte, mixing of the trachyte with the basalt should therefore also produce the basaltic andesite.

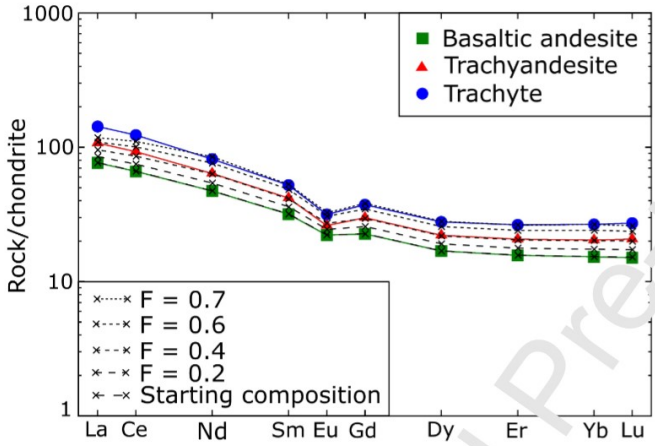

Figure 14: REE profiles of modelled compositions (black crosses) generated by batch fractionation of 28% olivine, 20% clinopyroxene, 32% plagioclase and 20% Magnetite from a basaltic andesite (green squares) lava from Quetrupillán. Different degrees of fractionation (F) are denoted by different styles of dashed lines. REE profiles of trachyte (blue circles) and trachyandesite (red triangles) lavas from Quetrupillán are also included.

5.5. Tectonic constraints

Our proposed model for the tectonic setting at Quetrupillán (Figure 15) is based on Quetrupillán's location in relation to the geometry of the LOFZ in the area. Dextral strike-slip movement along the branches of the LOFZ would result in the central block undergoing rotation, leading to zones of compression and tension within the block. The dextral-oblique convergence between the Nazca and South American Plates has resulted in a maximum compression axis (σ_1) that is subhorizontal and NE-trending in the SVZ, while the minimum compression axis (σ_3) is subhorizontal and NW-trending (Cembrano and Lara, 2009).

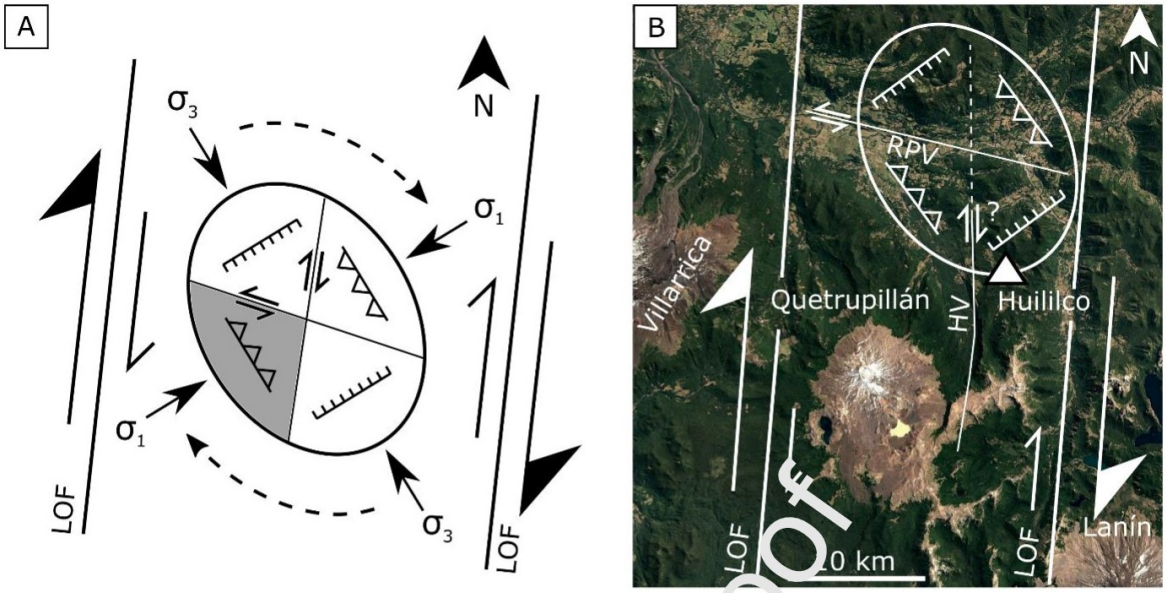

Figure 15: A) The proposed tectonic model for Quetrupillán, based on the ellipse of deformation from Rosenau et al. (2006). The grey region shows where we propose Quetrupillán is located, on a rotating block between the two NNE-trending dextral strike-slip Liquiñe-Ofqui faults (LOF). B) The proposed tectonic model superimposed over aerial imagery of the Villarrica-Lanín volcanic chain. A fault is suspected along the Huililco Valley (HV) due to the N-trending scarp to the east of Quetrupillán. Consistent with this model, a sinistral strike-slip fault is inferred in the Rio Pucón Valley (RPV) to the north of Quetrupillán, and is outlined by Rosenau et al. (2006). Volcán Huililco is denoted in the figure by a triangle. Satellite image from Google Earth (downloaded 26/05/2020).

Assuming Quetrupillán is located in the southwest compressive quadrant, then the theoretical N-S strike-slip fault in the model matches the ~N-S aligned fault scarp that runs along the Huililco Valley. If so, Volcán Huililco (a basaltic scoria cone) would be located in the southeast extensional quadrant, as it is on the other side of the Huililco Valley fault scarp. The theoretical W-E strike-slip fault on our model could be matched with the strike-slip fault running ~NW-SE along the Rio Pucón Valley, north of Quetrupillán, defined by Rosenau et al. (2006).

Tectonically, Quetrupillán has a unique position among the Holocene volcanoes of the SVZ as it is located between the two main branches of the LOFZ (Figure 1). According to Cembrano and Lara (2009), Quetrupillán and Sollipulli are the only stratovolcanoes that lie between the two branches of the LOFZ. Sollipulli, which lies 60 km north of Quetrupillán, is the closest analogue volcano to Quetrupillán in terms of being a volcanic complex in the same tectonic position, sitting between the branches of the LOFZ. However, we know of no study that links the tectonic and magmatic interplay at Sollipulli, and so we are unable to compare whether similar structural controls have influenced its magmatism. Although its overall volcano-tectonic setting will be different from Quetrupillán, it

seems likely that similar tectonic stresses have also influenced magmatism at Sollipulli. Erupted products from Sollipulli show a range of enrichment (Figure 10), suggesting they have undergone different degrees of contamination and evolution, controlled by the tectonic stresses at the volcano.

Observed lineaments around the flanks of Quetrupillán are predominantly oriented tangentially to the main edifice, with very few oriented radially to it (Figure 8). The load imposed by a volcanic edifice on the crust will cause stress perturbations that are expected to result in dykes and fissures with trajectories that are radial to the edifice summit, while beyond the influence of the volcanic edifice any lineaments are expected to be oriented to the regional stress regime (Roman and Jaupart, 2014).

At Volcán Llaima, 90 km north of Quetrupillán, the influence of the tectonic regime is superimposed on the influence of the volcanic edifice, resulting in two sets of dykes, one oriented radial to the summit and one oriented to the stress regime generated by the relative location of the LOFZ (Schonwalder-Angel et al., 2018). At Quetrupillán, the absence of radially oriented lineaments strongly suggests that the regional stress regime generated by the LOFZ overwhelms the local stress perturbations caused by the volcanic edifice. And unlike at Llaima (Schonwalder-Angel et al., 2018), there is no relation between the composition of products from vents on the flanks of Quetrupillán, and the location of the vents (Figure 2). This implies that although the orientation of lineaments is influenced by the tectonic regime, the variation in composition of volcanic products is not, suggesting that such variation is a consequence of a more localised process.

The secondary set of lineaments at Quetrupillán corresponds to the orientation of the LOFZ (NNE), while the primary set of lineaments seems to be a conjugate set to them (Figure 8). The dominant structures at other volcanoes located on or near the LOFZ show similar orientations to this, such as at Yate and Michinmahuida (Watt et al., 2009). This suggests that the stress field of the LOFZ may have a similar influence on the magmatic plumbing systems of other volcanoes within the SVZ.

5.6. Conceptual model

It is generally accepted that magmatic plumbing systems form stable transcrustal structures (Cashman et al., 2017; Magee et al., 2018). We adapt this conceptual model for the magmatic plumbing system of Quetrupillán, in which pockets of trachytic melt are contained within a region of crystal mush (Figure 16). Partial melting in the lithospheric mantle feeds basaltic melt into the base of the crust (Hildreth and Moorbath, 1988; Hickey-Vargas et al., 2016b; Magee et al., 2018), which stalls on its ascent through the crust due to the local compressional tectonic regime in which Quetrupillán is located (Figure 15). In accordance with this model, these pockets of stalled melt evolve through fractional crystallisation (Hickey-Vargas et al., 1989; Brahm et al., 2018), and as liquid

magma crystallises, the proportion of crystals suspended in the melt increases until they have formed a network of crystals containing interstitial melt, at which point they become crystal mush (Hildreth, 2004; Glazner et al., 2016). Crystallisation will result in an increased silica content in the remaining melt. It is proposed that a degree of crustal contamination will result in increased alkali and LILE concentrations, as well as enrichment in some of the HFSEs (Figure 7), producing the trachytic magmatic system present below Quetrupillán. The production of trachytes is regionally unusual (Stern, 2004), and is speculated to occur at Quetrupillán due to its unique tectonic setting.

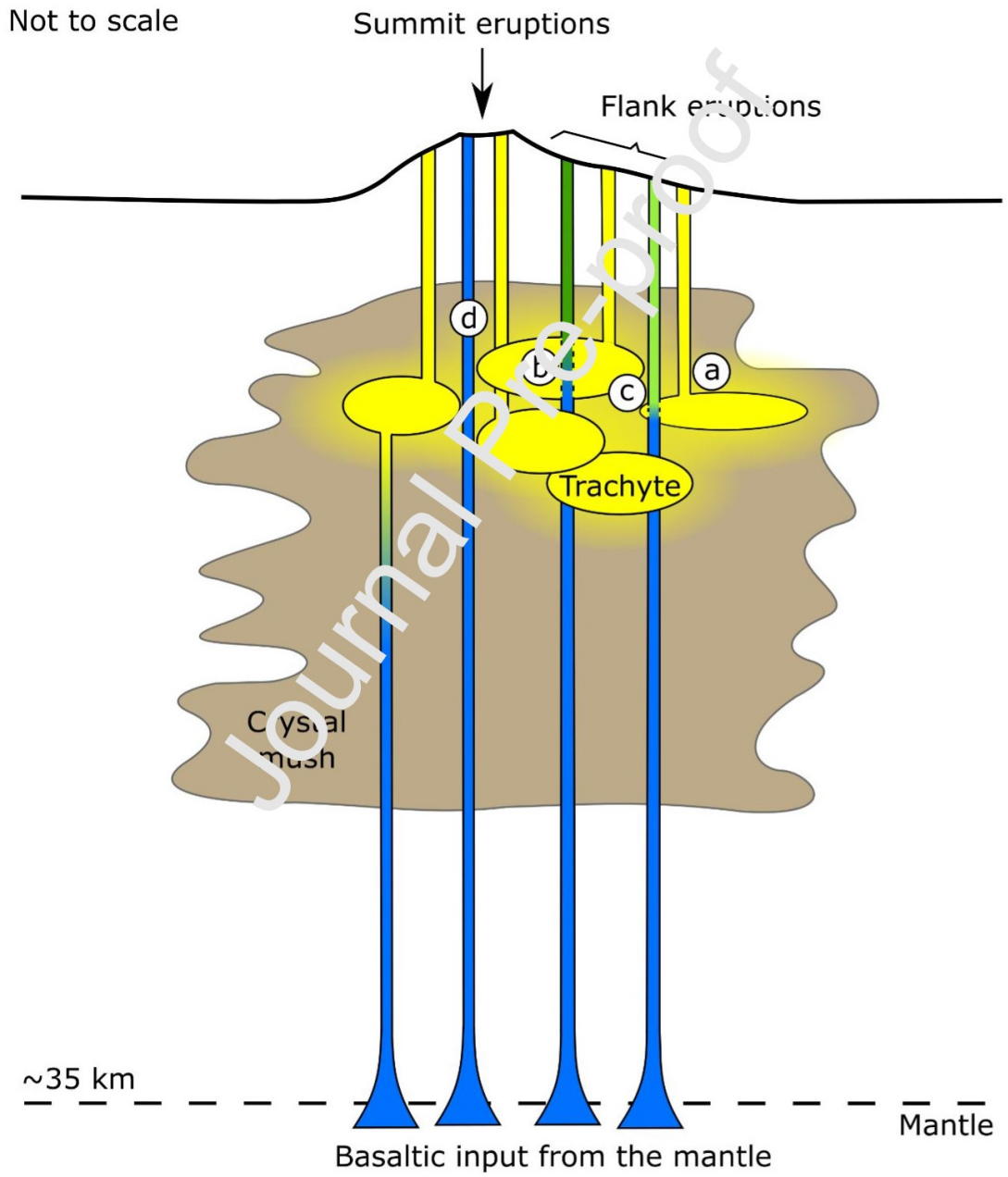

Figure 16: A conceptual model for the magmatic plumbing system below Quetrupillán, in which pockets of trachytic melt are contained within a region of crystal mush. Extraction of melt from

these pockets produces trachytic eruptions (a). Basaltic melt is injected into the system at the base of the crust, and if it ascends close to the surface with minimal interaction with the resident trachyte melts and mush, then trachyandesite (b), basaltic andesite (c) and basalt (d) melts will be produced and erupted, depending on the degree of interaction and mixing.

Partial melting in the mantle generates the basaltic melt that is injected into the base of the crust at all the magmatic plumbing systems in the SVZ (Hildreth and Moorbath, 1988). The local tectonic regime at each volcano will control how fast this basalt ascends through the crust, determining whether it will evolve to more differentiated compositions (Cembrano and Lara, 2009). At Volcán Villarrica, there is a continual flux of magma through the system. As one of the most active volcanoes in South America (Lara, 2004; Petit-Breuilh, 2004), the basaltic input is rapidly fluxed through the magmatic plumbing system and so does not evolve beyond basaltic andesite. This suggests that the stress conditions to the west of the LOFZ promote magma ascent, while within the LOFZ magma ascent is hindered. If an equivalent rate of basaltic injection is occurring beneath Quetrupillán as beneath Villarrica, then the tectonic setting at Quetrupillán is preventing it from fluxing through the system so rapidly. Instead, the melt stalls below Quetrupillán, where it evolves into the trachytic plumbing system.

Most basaltic magma that is injected into the base of the magmatic plumbing system will stall within the plumbing system, either in a melt pocket or in the crystal mush, where it will evolve and/or mix with the established trachytic resident melts. While most injected basalt transported by deeply sourced feeder dykes will encounter melt pockets and mingle with the existing magma, some will reach the surface with only minimal interaction with the resident melts (Pansino and Taisne, 2019). The degree of interaction will control the extent of mixing, determining whether the resultant hybrid magma is basaltic andesite (>~60% basalt mixed with <~40% trachyte) or trachyandesite (<~60% basalt mixed with >~40% trachyte). The varying degrees of interaction may reflect whether ascending basalt intersects the thicker centre of a trachyte pocket (labelled “b” in Figure 16) or the thinner margin (labelled “c” in Figure 16), or whether ascending basalt intersects multiple stacked pockets. The eruption of basaltic lavas suggests that some rising basaltic magma had no interaction with trachytic melt pockets during its ascent (labelled “d” in Figure 16), retaining its basaltic composition when reaching the surface.

In trachyte lavas, the variations in the compositions of melt inclusions, groundmass glass and plagioclase suggest variations in the composition of the melts from which the trachyte lavas have been sourced. Each trachytic melt pocket in the magmatic system will evolve with a slightly different composition, and extraction of melt from different pockets will result in the slight differences observed in trachytic erupted products. This implies slight variations in the composition of the

trachyte end members that mixed with ascending basalt to produce the hybrid basaltic andesite and trachyandesite lavas, explaining the range in melt inclusion compositions found in clinopyroxene xenocrysts.

The Holocene basalt erupted from the summit region and used in the modelled magma mixing is a good approximation for the composition of the source basalt that was input into the base of the system. The similarity in the range of erupted products through the Pleistocene and Holocene (Figure 3) suggests that there has been no significant change in magma production through time, implying that Quetrupillán's magmatic plumbing system is a stable feature that was established by the Pleistocene.

6. Conclusions

The plumbing system of Quetrupillán has developed as a transcrustal magmatic system composed of pockets of trachytic melt within a crystal mush, generated by fractional crystallisation and crustal contamination of the basaltic melt injected into the system. Quetrupillán's location within the LOFZ results in compressive tectonic stresses that hinder magma ascent and so promote stalling and evolution of melt within the crust. The tectonic stresses imposed by the LOFZ have a greater influence than the stresses imposed by the load of the volcanic edifice, resulting in lineaments that are tangential to the main edifice, rather than radial to it. Dyke formation enables evolved, trachytic melts to be extracted from the pockets of the magmatic plumbing system and ascend to the surface, forming the numerous trachytic eruptions that have occurred from Quetrupillán's summit and flanks during the Holocene. In some cases, basaltic melt is transported through the system with only minimal interaction with the settled trachytic plumbing system. Varying degrees of mixing between basalt and trachyte produce the basalt, basaltic andesite and trachyandesite products that have been erupted from Quetrupillán.

Data availability

The Supplementary Material contains XRF analyses (collected during this study, and data used in this study collected by other authors), mineral analyses, sample locations and geothermobarometry data.

Author contributions

Isla Simmons: Investigation, Writing – original draft, Writing – review and editing. Joaquín Cortés: Investigation, Writing – original draft, Writing – review and editing, Supervision. Dave McGarvie: Investigation, Writing – review and editing, Supervision. Eliza Calder – Supervision.

Declaration of competing interest

The authors declare that they have no competing interests.

Acknowledgements

The work in this paper forms part of a NERC-funded PhD studentship by Isla Simmons (Grant number NE/L002558/1). Joaquín Cortés received funding from Edge Hill University (RIF grant 1CORTE18) and Santander Universities supported Dave McGarvie. Huge thanks to John Simmons, Franco Vera Rivadeneira, Jack McGarvie and Jonathan Moles for being fantastic field assistants, and to Christa Bönninghoff, Cristian Silva and Claudia Guzmán Roa for help with logistics in the field. We thank Nic Odling, Mike Hall, Nicola Cayzer, Chris Hayward and John Craven at the University of Edinburgh and Valerie Olive at SUERC for analytical support. And thank you to Sebastian Watt and an anonymous reviewer for comments that greatly improved this manuscript, and to Diana Roman for editorial handling.

References

Allmendinger, R.W., Cardozo, N.C., Fisher, D., 2013. Structural Geology Algorithms: Vectors & Tensors. Cambridge University Press.

Brahm, R., Parada, M.A., Morgado, E., Contreras, C., McGee, L.E., 2018. Origin of Holocene trachyte lavas of the Quetrupillán volcanic complex, Chile: Examples of residual melts in a rejuvenated crystalline mush reservoir. J. Volcanol. Geotherm. Res. 357, 163–176. doi:10.1016/j.jvolgeores.2018.04.025

Cameron, M., Papike, J.J., 1981. Structural and chemical variations in pyroxenes. Am. Mineral. 66, 1–50.

Cardozo, N.C., Allmendinger, R.W., 2013. Spherical projections with OSXStereonet. Comput. Geosci. 51, 193–205. doi:10.1016/j.cageo.2012.07.021

Carmichael, I.S.E., Nicholls, J., Smith, A.L., 1970. Silica Activity in Igneous Rocks. Am. Mineral. 55, 246–263.

Cashman, K. V., Sparks, R.S.J., Blundy, J.D., 2017. Vertically extensive and unstable magmatic systems: A unified view of igneous processes. Science (80-.). 355. doi:10.1126/science.aag3055

Cembrano, J., Hervé, F., Lavenu, A., 1996. The Liquiñe Ofqui fault zone: a long-lived intra-arc fault system in southern Chile. Tectonophysics 259, 55–66. doi:10.1016/0040-1951(95)00066-6

Cembrano, J., Lara, L., 2009. The link between volcanism and tectonics in the southern volcanic zone of the Chilean Andes: A review. Tectonophysics 471, 96–113. doi:10.1016/j.tecto.2009.02.038

Cembrano, J., Schermer, E., Lavenu, A., Sanhueza, A., 2000. Contrasting nature of deformation along

an intra-arc shear zone, the Liquine-Ofqui fault zone, southern Chilean Andes. Tectonophysics 319, 129–149. doi:10.1016/S0040-1951(99)00321-2

Clavero, J., Moreno, H., 2004. Evolution of Villarrica Volcano, in: Lara, L., Clavero, J. (Eds.), Villarrica Volcano (39.5°S), Southern Andes, Chile. Servicio Nacional de Geología y Minería, pp. 17–27.

Cortés, J.A., 2019. Strike converter 1.0 for ImageJ.

Cortés, J.A., 2016. Olive.

Cortés, J.A., Wilson, M., Condliffe, E., Francalanci, L., 2006. The occurrence of forsterite and highly oxidizing conditions in basaltic lavas from Stromboli volcano, Italy. J. Petrol. 47, 1345–1373. doi:10.1093/petrology/egl012

Daly, R.A., 1911. The Nature of Volcanic Action. Proc. Am. Acad. Arts Sci. 47, 47–122.

Danyushevsky, L. V., Plechov, P., 2011. Petrolog3: Integrated software for modeling crystallization processes. Geochemistry, Geophys. Geosystems 12. doi:10.1029/2011GC003516

Ginibre, C., Wörner, G., Kronz, A., 2002. Minor- and trace-element zoning in plagioclase: Implications for magma chamber processes at Parinacota volcano, northern Chile. Contrib. to Mineral. Petrol. 143, 300–315. doi:10.1007/s00410-002-0351-z

Glazner, A., Bartley, J., Coleman, D., 2016. We Need a New Definition for "Magma." Eos (Washington. DC). 97, 1–7. doi:10.1029/2016eo059741

Gudmundsson, A., 2012. Magma chambers: Formation, local stresses, excess pressures, and compartments. J. Volcanol. Geotherm. Res. 237–238, 19–41. doi:10.1016/j.jvolgeores.2012.05.015

Hernandez-Moreno, C., Speranza, F., Di Chiara, A., 2014. Understanding kinematics of intra-arc transcurrent deformation: Paleomagnetic evidence from the Liquiñe-Ofqui fault zone (Chile, 38–41°S). Tectonics 33, 1964–1988. doi:10.1002/2014TC003622

Hersum, T.G., Marsh, B.D., 2007. Igneous textures: On the kinetics behind the words. Elements 3, 247–252. doi:10.2113/gselements.3.4.247

Hervé, F., 1994. The Southern Andes between 39° and 44°S latitude: The geological signature of a transpressive tectonic regime related to a magmatic arc, in: Reutter, K.J., Scheuber, E., Wigger, P.J. (Eds.), Tectonics of the Southern Central Andes. Springer, Berlin, pp. 243–248. doi:10.1007/978-3-642-77353-2_17

Hickey-Vargas, R., Holbik, S., Tormey, D., Frey, F.A., Moreno Roa, H., 2016a. Basaltic rocks from the Andean Southern Volcanic Zone: Insights from the comparison of along-strike and small-scale

geochemical variations and their sources. Lithos 258–259, 115–132. doi:10.1016/j.lithos.2016.04.014

Hickey-Vargas, R., Moreno, H., Lopez-Escobar, L., Frey, F.A., 1989. Geochemical variations in Andean basaltic and silicic lavas from the Villarrica-Lanín volcanic chain (39.5° S): an evaluation of source heterogeneity, fractional crystallization and crustal assimilation. Contrib. to Mineral. Petrol. 103, 361–386. doi:10.1007/BF00402922

Hickey-Vargas, R., Sun, M., Holbik, S., 2016b. Geochemistry of basalts from small eruptive centers near Villarrica stratovolcano, Chile: Evidence for lithospheric mantle components in continental arc magmas. Geochim. Cosmochim. Acta 185, 358–382. doi:10.1016/j.gca.2016.03.033

Hickey-Vargas, R., Sun, M., López-Escobar, L., Moreno-Roa, H., Reagan, M.K., Morris, J.D., Ryan, J.G., 2002. Multiple subduction components in the mantle wedge: Evidence from eruptive centers in the Central Southern volcanic zone, Chile. Geology 30, 199–202. doi:10.1130/0091-7613(2002)030<0199:MSCITM>2.0.CO;2

Hildreth, W., 2004. Volcanological perspectives on Long Valley, Mammoth Mountain, and Mono Craters: Several contiguous but discrete systems. J. Volcanol. Geotherm. Res. 136, 169–198. doi:10.1016/j.jvolgeores.2004.05.019

Hildreth, W., Moorbath, S., 1988. Crustal contributions to arc magmatism in the Andes of Central Chile. Contrib. to Mineral. Petrol. 98, 455–489. doi:10.1007/BF00372365

Irvine, T.N., Baragar, W.R.A., 1971. A guide to the chemical classification of the common volcanic rocks. Can. J. Earth Sci. 8, 523–548. https://doi.org/doi:10.1139/e71-055

Lara, 2004. Overview of Villarrica Volcano, in: Lara, L., Clavero, J. (Eds.), Villarrica Volcano (39.5°S), Southern Andes, Chile. Servicio Nacional de Geología y Minería, pp. 5–12.

Lara, L.E., Lavenu, A., Cembrano, J., Rodríguez, C., 2006. Structural controls of volcanism in transversal chains: Resheared faults and neotectonics in the Cordón Caulle-Puyehue area (40.5°S), Southern Andes. J. Volcanol. Geotherm. Res. 158, 70–86. doi:10.1016/j.jvolgeores.2006.04.017

Lara, L.E., Naranjo, J.A., Moreno, H., 2004. Lanín volcano (39.5°S), Southern Andes: geology and morphostructural evolution. Rev. Geológica Chile 31, 1–14. doi:10.4067/S0716-02082004000200004

Le Maitre, R.W., Streckeisen, A., Zanettin, B., Le Bas, M.J., Bonin, B., Bateman, P., 2002. Igneous Rocks; A Classification and Glossary of Terms, 2nd ed. Cambridge University Press.

López-Escobar, L., Cembrano, J., Moreno, H., 1995. Geochemistry and tectonics of the Chilean southern Andes basaltic Quaternary volcanism (37-46°S). Rev. Geológica Chile 22, 219–234. doi:10.5027/andgeoV22n2-a06

Lorenz, V., 1986. On the growth of maars and diatremes and its relevance to the formation of tuff rings. Bull. Volcanol. 265–274. doi:10.1007/BF01081755

Magee, C., Stevenson, C.T.E., Ebmeier, S.K., Keir, D., Hammond, J.O.S., Gottsmann, J.H., Whaler, K.A., Schofield, N., Jackson, C.A.L., Petronis, M.S., O'Driscoll, B., Morgan, J., Cruden, A., Vollgger, S.A., Dering, G., Micklethwaite, S., Jackson, M.D., 2018. Magma plumbing systems: A geophysical perspective. J. Petrol. 59, 1217–1251. doi:10.1093/petrology/egy064

Marsh, B.D., 1989. Magma chambers. Annu. Rev. earth Planet. Sci. Vol. 17 439–474. doi:10.1146/annurev.earth.17.1.439

McGarvie, D.W., Macdonald, R., Pinkerton, H., Smith, R.L., 1990. Petrogenetic evolution of the torfajökull volcanic complex, Iceland II. The role of magma mixing. J. Petrol. 31, 461–481. doi:10.1093/petrology/31.2.461

McGarvie, Dave, Pavez, A., Cortés, J.A., Faggetter, L., Burgess, R., McGarvie, Dan, 2014. Glaciovolcanism at Volcán Quetrupillán, Chile, in: GSA Annual Meeting.

McGee, L.E., Brahm, R., Rowe, M.C., Handley, H.K., Morgado, E., Lara, L.E., Turner, M.B., Vinet, N., Parada, M.Á., Valdivia, P., 2017. A geochemical approach to distinguishing competing tectono-magmatic processes preserved in small eruptive centres. Contrib. to Mineral. Petrol. 172, 1–26. doi:10.1007/s00410-017-1362-2

Nelson, S.T., Montana, A., 1992. Sieve-textured plagioclase in volcanic rocks produced by rapid decompression. Am. Mineral. 77, 1242–1249.

Nimis, P., 1999a. Clinopyroxene geobarometry of magmatic rocks. Part 2. Structural geobarometers for basic to acid, tholeiitic and mildly alkaline magmatic systems. Contrib. to Mineral. Petrol. 135, 62–74. doi:10.1007/s004100050498

Nimis, P., 1999b. CpxBar Excel version.

Olive, V., Ellam, R.M., Wilson, L., 2001. A protocol for the determination of the rare earth elements at picomole level in rocks by ICP-MS: Results on geological reference materials USGS PCC-1 and DTS-1. Geostand. Newsl. 25, 219–228. doi:10.1111/j.1751-908x.2001.tb00597.x

Pansino, S., Taisne, B., 2019. How Magmatic Storage Regions Attract and Repel Propagating Dikes. J. Geophys. Res. Solid Earth 124. doi:10.1029/2018JB016311

Papike, J.J., Cameron, K.L., Baldwin, K., 1974. Amphiboles and pyroxenes: Characterization of Other than quadrilateral components and estimates of ferric iron from microprobe data. Geol. Soc. Am. Abstr. with Programs 6, 1053–1054.

Pardo-Casas, F., Molnar, P., 1987. Relative motion of the Nazca (Farallon) and South American plates since Late Cretaceous time. Tectonics 6, 233–248.

Pavez, A., 1997. Geología e historia evolutiva del Complejo Volcánico Quetrupillán, Andes del Sur, 39.5° L.S., in: VIII Congreso Geológico Chileno. pp. 1443–1447.

Pearce, J.A., 1983. Role of the sub-continental lithosphere in magma genesis at active continental margins, in: Hawkesworth, C.J., Norry, M.J. (Eds.), Continental Basalts and Mantle Xenoliths. Shive Publications, Nantwich, Cheshire, pp. 230–249.

Petit-Breuilh, M.E., 2004. La historia eruptiva de los volcanes Hispanoamericanos (Siglos XVI al XX). Cabildo Insular de Lanzarote.

Putirka, K.D., 2008. Thermometers and Barometers for Volcanic Systems. Rev. Mineral. Geochemistry 69, 61–120. doi:10.2138/rmg.2008.69.3

Roeder, P.L., Emslie, R.F., 1970. Olivine-liquid equilibrium. Contrib. to Mineral. Petrol. 29, 275–289.

Rollinson, H., 1993. Using geochemical data: evaluation, presentation, interpretation. Routledge.

Roman, A., Jaupart, C., 2014. The impact of a volcanic edifice on intrusive and eruptive activity. Earth Planet. Sci. Lett. 408, 1–8. doi:10.1016/j.epsl.2014.09.016

Rosenau, M., Melnick, D., Echtler, H., 2006. Kinematic constraints on intra-arc shear and strain partitioning in the southern Andes between 38°S and 42°S latitude. Tectonics 25. doi:10.1029/2005TC001943

Schindelin, J., Arganda-Carreras, I., Frise, E., Kaynig, V., Longair, M., Pietzsch, T., Preibisch, S., Rueden, C., Saalfeld, S., Schmid, B., Tinevez, J.Y., White, D.J., Hartenstein, V., Eliceiri, K., Tomancak, P., Cardona, A., 2012. Fiji: An open-source platform for biological-image analysis. Nat. Methods 9, 676–682. doi:10.1038/nmeth.2019

Schonwalder-Angel, D., Cortés, J.A., Calder, E.S., 2018. The interplay of magmatism and tectonics: An example based on the satellite scoria cones at Llaima volcano, Chile. J. Volcanol. Geotherm. Res. 367, 31–45. doi:10.1016/j.jvolgeores.2018.10.020

Simmons, I.C., McGarvie, D., Cortés, J.A., Calder, E.S., Pavez, A., 2020. Holocene volcanism at the Quetrupillán Volcanic Complex (39°30’ S, 71°43’ W), southern Chile. Volcanica 3, 115–137. doi:10.30909/vol.03.01.115137

Sisson, T.., Grove, T.L., 1993. Temperatures and H2O contents of low-MgO high-alumina basalts. Contrib. to Mineral. Petrol. 113, 167–184.

Stern, C.R., 2004. Active Andean volcanism: Its geologic and tectonic setting. Rev. Geológica Chile 31, 161–206. doi:10.4067/S0716-02082004000200001

Stern, C.R., 1991. Role of subduction erosion in the generation of Andean magmas. Geology 19, 78–81. doi:10.1130/0091-7613(1991)019<0078:ROSEIT>2.3.CO;2

Stern, C.R., Moreno, H., Lopéz-Escobar, L., Clavero, J.E., Lara, L.E., Naranjo, J.A., Parada, M.A., Skewes, M.A., 2007. Chilean Volcanoes, in: Moreno, T., Gibbons, W. (Eds.), The Geology of Chile. Geological Society of London Special Publication, pp. 147–178. https://doi.org/doi:10.1144/GOCH.5

Sun, S.S., McDonough, W.F., 1989. Chemical and isotopic systematics of oceanic basalts: Implications for mantle composition and processes. Geol. Soc. Spec. Publ. 42, 313–345. doi:10.1144/GSL.SP.1989.042.01.19

Toplis, M.J., Carroll, M.R., 1995. An experimental study of the influence of oxygen fugacity on fe-ti oxide stability, phase relations, and mineral-melt equilibria in ferro-basaltic systems. J. Petrol. 36, 1137–1170. doi:10.1093/petrology/36.5.1137

Valentine, G.A., Connor, C.B., 2015. Basaltic Volcanic Fields, Second Edi. ed, The Encyclopedia of Volcanoes. Elsevier Inc. doi:10.1016/B978-0-12-385938-9.00023-7

Valentine, G.A., Gregg, T.K.P., 2008. Continental basaltic volcanoes - Processes and problems. J. Volcanol. Geotherm. Res. doi:10.1016/j.jvolgeores.2008.01.050

Watt, S.F.L., Pyle, D.M., Naranjo, J.A., Mather, T.A., 2009. Landslide and tsunami hazard at Yate volcano, Chile as an example of edifice destruction on strike-slip fault zones. Bull. Volcanol. 71, 559–574. doi:10.1007/s00445-008-0242-x

Weidmann, C., Spagnotto, S., Giménez, M., Martínez, P., Álvarez, O., Sánchez, M., Lince Klinger, F., 2013. Crustal structure and tectonic setting of the south central Andes from gravimetric analysis. Geofis. Int. 52, 197–208. doi:10.1016/S0016-7169(13)71472-7

Wilson, S.A., 1997. The collection, preparation and testing of USGS reference material BCR-2, Columbia River Basalt.

Wohletz, K.H., Sheridan, M.F., 1983. Hydrovolcanic explosions II. Evolution of basaltic tuff rings and tuff cones. Am. J. Sci. 283, 385–413. doi:10.2475/ajs.283.5.385

Table captions

Table 1: Whole rock geochemical analyses of representative samples from Quetrupillán. Major element analyses are in wt.% and trace element analyses are in ppm. Some trace elements were not determined (n.d.) or below detection limit (b.d.l.). Samples marked * were analysed by ICP-MS for La, Ce, Pr, Nd, Sm, Eu, Gd, Tb, Dy, Ho, Er, Tm, Yb, Lu, Hf, Pb, Th and U. All other analyses were done by XRF. Results of all samples analysed during this study are available in the supplementary material.

Table 2: Mineral analyses of representative minerals from samples of Quetrupillán lavas. Analyses were made by EMPA and are in wt.%. Cations per formula unit (c.f.u.) were recalculated based on the number of oxygen (N.O.). Some elements were below detection limit (b.d.l.). Results of all mineral analyses are available in the supplementary material. Speciation of iron was estimated following Papike et al. (1974).

Sample	Q3*	Q8*	Q50*	Q62	Q60	Q63	Q67	Q26
Comp.	Trachyte	Trachy-andesite	Basaltic andesite	Trachyte	Trachy-andesite	Basaltic andesite	Basalt	Trachyte
Source /type	Flank	Flank	Flank	Summit	Summit	Summit	Summit	Tephra
SiO_2	64.96	58.66	54.84	63.56	58.25	55.37	51.93	64.34
TiO_2	1.11	1.36	1.04	1.24	1.17	1.06	1.06	1.14
Al_2O_3	15.36	16.17	16.23	14.97	16.08	16.03	17.87	15.51
$Fe_2O_3^T$	5.54	8.16	8.80	6.39	7.64	8.01	8.97	5.71
MnO	0.13	0.13	0.14	0.13	0.13	0.14	0.15	0.13
MgO	1.21	2.89	6.50	1.39	3.49	5.12	6.37	1.26
CaO	3.11	5.88	7.67	3.48	5.96	6.94	9.33	3.33
Na_2O	4.85	3.92	3.22	4.51	3.80	3.32	3.02	4.74
K_2O	3.05	2.34	1.48	3.16	2.31	1.74	1.01	2.95
P_2O_5	0.33	0.36	0.28	0.43	0.35	0.28	0.31	0.35
LOI	0.20	-0.02	-0.21	-0.06	-0.14	-0.04	-0.21	0.30
Total	99.84	99.84	100.00	99.19	99.04	97.96	99.80	99.77
Sc	16.6	24.3	27.3	18.9	22.4	24.7	28.1	17.4
V	63.7	228.8	210.5	95.7	172.6	192.8	214.4	70.4
Cr	4.0	28.2	179.8	3.1	59.9	154.9	164.9	4.3
Ni	b.d.l.	18.6	78.3	1.3	27.8	66.2	66.4	b.d.l.
Cu	14.5	59.9	56.7	21.0	46.3	44.1	63.2	15.5
Zn	71.2	76.1	74.4	75.9	69.9	68.7	65.7	75.4
Rb	77.8	60.3	36.2	82.1	60.4	43.9	22.0	74.7
Sr	284.3	371.8	429.4	276.9	389.5	403.5	568.1	301.7
Y	44.4	36.9	27.5	47.7	35.7	30.2	22.9	43.9
Zr	352.2	270.6	174.3	378.9	271.8	205.6	124.1	334.6
Nb	14.1	10.9	7.4	15.2	11.2	8.5	6.8	13.2
Ba	737.8	583.2	383.0	713.1	553.2	445.1	334.8	729.7

La	33.82	25.46	18.16	35.9	25.6	19.4	14.3	32.3
Ce	75.53	56.85	40.52	83.8	60.4	47.8	39.4	79.7
Pr	9.32	7.16	5.21	n.d.	n.d.	n.d.	n.d.	n.d.
Nd	37.31	29.12	21.59	42.0	32.3	24.5	20.3	39.2
Sm	7.73	6.20	4.70	n.d.	n.d.	n.d.	n.d.	n.d.
Eu	1.78	1.47	1.25	n.d.	n.d.	n.d.	n.d.	n.d.
Gd	7.43	5.95	4.51	n.d.	n.d.	n.d.	n.d.	n.d.
Tb	1.13	0.91	0.70	n.d.	n.d.	n.d.	n.d.	n.d.
Dy	6.84	5.44	4.16	n.d.	n.d.	n.d.	n.d.	n.d.
Ho	1.39	1.10	0.84	n.d.	n.d.	n.d.	n.d.	n.d.
Er	4.23	3.31	2.51	n.d.	n.d.	n.d.	n.d.	n.d.
Tm	0.69	0.52	0.39	n.d.	n.d.	n.d.	n.d.	n.d.
Yb	4.29	3.28	2.46	n.d.	n.d.	n.d.	n.d.	n.d.
Lu	0.67	0.51	0.37	n.d.	n.d.	n.d.	n.d.	n.d.
Hf	7.89	5.77	3.76	n.d.	n.d.	n.d.	n.d.	n.d.
Pb	24.74	17.54	11.19	n.d.	n.d.	n.d.	n.d.	21.3
Th	9.88	7.13	4.31	n.d.	n.d.	n.d.	n.d.	9.7
U	2.71	1.99	1.22	n.d.	n.d.	n.d.	n.d.	2.7

Table 1: Whole rock geochemical analyses of representative samples from Quetrupillán. Major element analyses are in wt.% and trace element analyses are in ppm. Some trace elements were not determined (n.d.) or below detection limit (b.d.l.). Samples marked * were analysed by ICP-MS for La, Ce, Pr, Nd, Sm, Eu, Gd, Tb, Dy, Ho, Er, Tm, Yb, Lu, Hf, Pb, Th and U. All other analyses were done by XRF. Results of all samples analysed during this study are available in the supplementary data.

Mineral	Augite	Augite	Augite	Augite	Augite	Augite	Enstatite	Enstatite	Enstatite	Pi
Analysis	Core	Core	Core	Core	Core	Core	Core	Core	Core	M
Lava composition	Basaltic andesite	Basaltic andesite	Trachy-andesite	Trachy-andesite	Trachyte	Trachyte	Trachy-andesite	Trachyte	Trachyte	Tr
Sample	Q50	Q50	Q8	Q8	Q3	Q3	Q8	Q3	Q3	
SiO_2	51.90	52.38	50.44	51.87	51.81	51.44	53.58	52.38	52.94	
TiO_2	0.71	0.58	0.72	0.72	0.83	0.66	0.40	0.32	0.46	
Al_2O_3	2.03	1.51	1.93	2.01	2.02	1.60	0.94	0.58	1.18	
FeO^T	9.64	9.79	9.34	9.34	10.57	11.49	18.54	19.47	20.90	
MnO	0.26	0.30	0.30	0.29	0.48	0.57	0.45	0.72	0.79	
MgO	14.17	13.77	15.50	13.70	14.73	13.70	22.60	23.73	21.00	
NiO	0.02	0.03	b.d.l.	0.02	b.d.l.	b.d.l.	0.04	b.d.l.	b.d.l.	
CaO	20.38	20.38	20.07	20.35	20.17	18.89	1.97	1.80	2.06	
Na_2O	0.32	0.32	0.32	0.30	0.37	0.32	0.03	0.03	0.04	
Total	99.42	99.05	98.61	98.59	100.98	98.67	98.55	99.03	99.37	
N.O.	6	6	6	6	6	6	6	6	6	
Si	1.9460	1.9711	1.9108	1.9578	1.9235	1.9563	1.9946	1.9581	1.9808	
Ti	0.0200	0.0164	0.0205	0.0204	0.0232	0.0189	0.0112	0.0090	0.0129	
Al	0.0897	0.0670	0.0862	0.0894	0.0884	0.0717	0.0412	0.0256	0.0520	
Fe^{3+}	0.0016	0.0000	0.0741	0.0000	0.0449	0.0015	0.0000	0.0424	0.0000	
Fe^{2+}	0.3007	0.3081	0.2218	0.2948	0.2833	0.3640	0.5772	0.5663	0.6540	
Mn	0.0083	0.0096	0.0096	0.0093	0.0151	0.0184	0.0142	0.0228	0.0250	

Mg	0.7921	0.7725	0.8754	0.7709	0.8153	0.7768	1.2543	1.3225	1.1714
Ni	0.0006	0.0009	0.0000	0.0006	0.0000	0.0000	0.0012	0.0000	0.0000
Ca	0.8186	0.8216	0.8145	0.8229	0.8022	0.7697	0.0786	0.0721	0.0826
Na	0.0233	0.0233	0.0235	0.0220	0.0266	0.0236	0.0022	0.0022	0.0029
Cation sum	4.00	3.99	4.04	3.99	4.02	4.00	3.97	4.02	3.98
Mg#	72	71	79	72	73	67	68	69	63

Table 2: Mineral analyses of representative minerals from samples of Quetrupillán lavas. Analyses were made by EMPA and are in wt.%. Cations per formula unit (c.f.u.) were recalculated based on the number of oxygen (N.O.). Some elements were below detection limit (b.d.l.). Results of all mineral analyses are available in the supplementary data. Speciation of iron was estimated following (Papike et al., 1974).

Mineral	Plagioclase (sieve)	Plagioclase (sieve)	Plagioclase (pristine)	Plagioclase (sieve)	Plagioclase (microlite)	Plagioclase (pristine)	Plagioclase (pristine)	Pl (p
Analysis	Core	Core	Core	Core	Microlite	Core	Middle	
Lava composition	Basaltic andesite	Basaltic andesite	Trachy-andesite	Trachy-andesite	Trachy-andesite	Trachyte	Trachyte	T
Sample	Q50	Q50	Q8	Q8	Q8	Q3	Q3	
SiO_2	49.42	53.90	52.10	47.43	56.56	57.95	56.91	
TiO_2	0.04	0.06	0.05	0.03	0.13	0.06	0.06	
Al_2O_3	31.44	28.16	29.99	32.99	25.22	26.38	27.00	
$Fe_2O_3^T$	0.67	0.65	0.73	0.71	1.16	0.53	0.54	
SrO	0.13	0.13	0.14	0.12	0.16	0.12	0.13	
MnO	b.d.l.	0.01	b.d.l.	b.d.l.	0.01	b.d.l.	0.01	
MgO	0.10	0.11	0.09	0.06	0.13	0.04	0.04	
CaO	15.18	11.35	13.56	17.32	8.94	8.88	9.71	
Na_2O	2.71	4.56	3.64	2.05	6.41	6.28	5.52	
K_2O	0.13	0.26	0.20	0.07	0.61	0.41	0.35	
Total	99.81	99.50	100.51	100.79	99.32	100.66	100.26	
N.O.	8	8	8	8	8	8	8	
Si	2.2691	2.4566	2.3645	2.1737	2.5805	2.5891	2.5547	
Ti	0.0014	0.0021	0.0017	0.0010	0.0045	0.0020	0.0020	
Al	1.7012	1.5125	1.6034	1.7818	1.3560	1.3890	1.4284	
Fe^{3+}	0.0231	0.0223	0.0249	0.0245	0.0397	0.0178	0.0182	
Sr	0.0035	0.0034	0.0037	0.0032	0.0042	0.0031	0.0034	
Mn	0.0000	0.0004	0.0000	0.0000	0.0004	0.0000	0.0004	
Mg	0.0068	0.0075	0.0061	0.0041	0.0088	0.0027	0.0027	
Ca	0.7467	0.5688	0.6591	0.8504	0.4370	0.4250	0.4670	
Na	0.2412	0.4029	0.3201	0.1821	0.5670	0.5440	0.4804	
K	0.0076	0.0151	0.0116	0.0041	0.0355	0.0234	0.0200	
Cation sum	5.00	4.99	5.00	5.03	5.04	5.00	4.98	
%An	75	58	67	82	42	43	48	

Mineral	Olivine	Olivine	Olivine	Olivine
Analysis	Core	Core	Core	Core
Lava composition	Basaltic andesite	Basaltic andesite	Trachy-andesite	Trachy-andesite
Sample	Q50	Q50	Q8	Q8
SiO_2	39.83	38.33	35.63	36.97
Al_2O_3	0.06	0.03	0.02	0.03
FeO	15.15	22.70	33.51	27.00
MnO	0.21	0.38	0.54	0.45
MgO	44.86	38.97	30.39	35.61
NiO	0.23	0.10	0.05	0.09
CaO	0.19	0.18	0.21	0.18
P_2O_5	0.04	0.05	0.05	b.d.l.
Total	100.58	100.74	100.40	100.34
N.O.	4	4	4	4
Si	0.9960	0.9924	0.9798	0.9827
Al	0.0018	0.0009	0.0006	0.0009
Fe^{2+}	0.3168	0.4915	0.7707	0.6208
Mn	0.0044	0.0083	0.0126	0.0101
Mg	1.6723	1.5042	1.2456	1.4125
Ni	0.0046	0.0021	0.0031	0.0019
Ca	0.0051	0.0050	0.0062	0.0051
P	0.0008	0.0011	0.0012	0.0000
Cation sum	3.00	3.01	3.02	3.02
%Fo	84	75	61	70

Mineral	Cr-spinel	Cr-spinel	Ilmenite	Ilmenite	Magnetite	Magnetite
Analysis	Core	Core	Core	Core	Core	Core
Lava composition	Basaltic andesite	Basaltic andesite	Trachyte	Trachyte	Trachyte	Trachyte
Sample	Q50	Q50	Q12	Q69	Q53	Q61
TiO_2	0.76	6.24	49.21	47.76	17.55	17.24
Al_2O_3	22.65	10.22	0.36	0.46	2.89	2.77
Cr_2O_3	30.05	21.63	b.d.l.	b.d.l.	b.d.l.	b.d.l.
FeO^T	37.14	55.49	46.28	46.85	75.79	76.04
MnO	b.d.l.	b.d.l.	b.d.l.	0.77	0.60	0.72
MgO	9.88	6.69	3.23	3.97	2.58	3.20
Total	100.48	100.27	99.08	99.81	99.41	99.97
N.O.	8	8	3	3	4	4
Ti	0.0373	0.3430	0.9396	0.9102	0.5321	0.5198
Al	1.7417	0.8801	0.0108	0.0137	0.1373	0.1308
Cr	1.5501	1.2495	0.0000	0.0000	0.0000	0.0000
Fe^{2+}	2.0266	3.3909	0.9823	0.9925	2.5544	2.5486

Mn	0.0000	0.0000	0.0000	0.0165	0.0205	0.0244
Mg	0.9611	0.7288	0.1222	0.1499	0.1550	0.1912
Cation sum	6.32	6.59	2.05	2.08	3.40	3.41

Author contributions

Isla Simmons: Investigation, Writing – original draft, Writing – review and editing.

Joaquín Cortés: Investigation, Writing – original draft, Writing – review and editing, Supervision.

Dave McGarvie: Investigation, Writing – review and editing, Supervision.

Eliza Calder – Supervision.

Declaration of interests

☒ The authors declare that they have no known competing financial interests or personal relationships that could have appeared to influence the work reported in this paper.

☐The authors declare the following financial interests/personal relationships which may be considered as potential competing interests:

Highlights

- Geochemical and textural data are a reflection of a volcanic plumbing system
- Quetrupillán's plumbing system consists of hybrid lenses of variable composition
- Regional tectonic stress overrides local stress, controlling the plumbing system's geometry

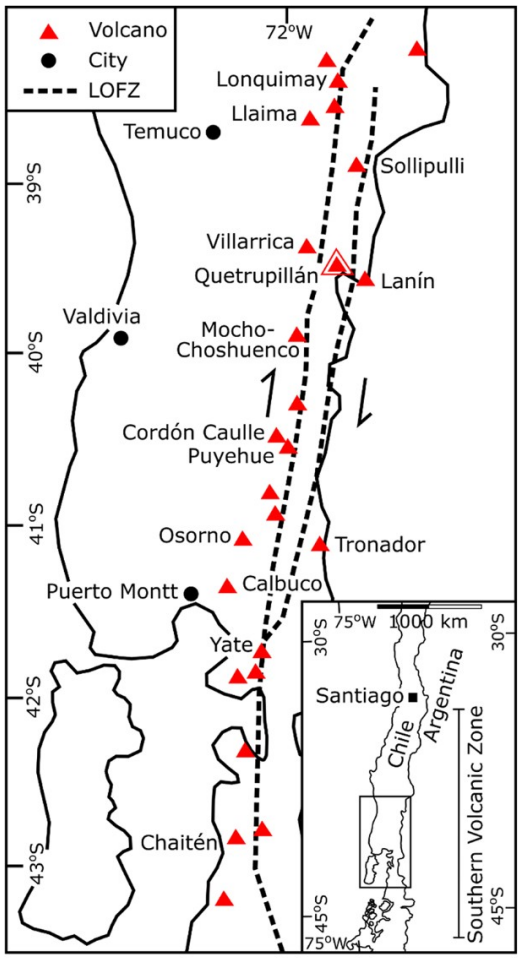
Volcano
City
LOFZ
72°W
Lonquimay
Llaima
Temuco
Sollipulli
39°S
Villarrica
Quetrupillán
Lanín
Valdivia
Mocho-
Choshuenco
40°S
Cordón Caulle
Puyehue
41°S
Osorno
Tronador
Puerto Montt
Calbuco
Yate
42°S
Chaitén
43°S
75°W 1000 km
30°S
Santiago
Chile
Argentina
Southern Volcanic Zone
45°S
75°W

Figure 1

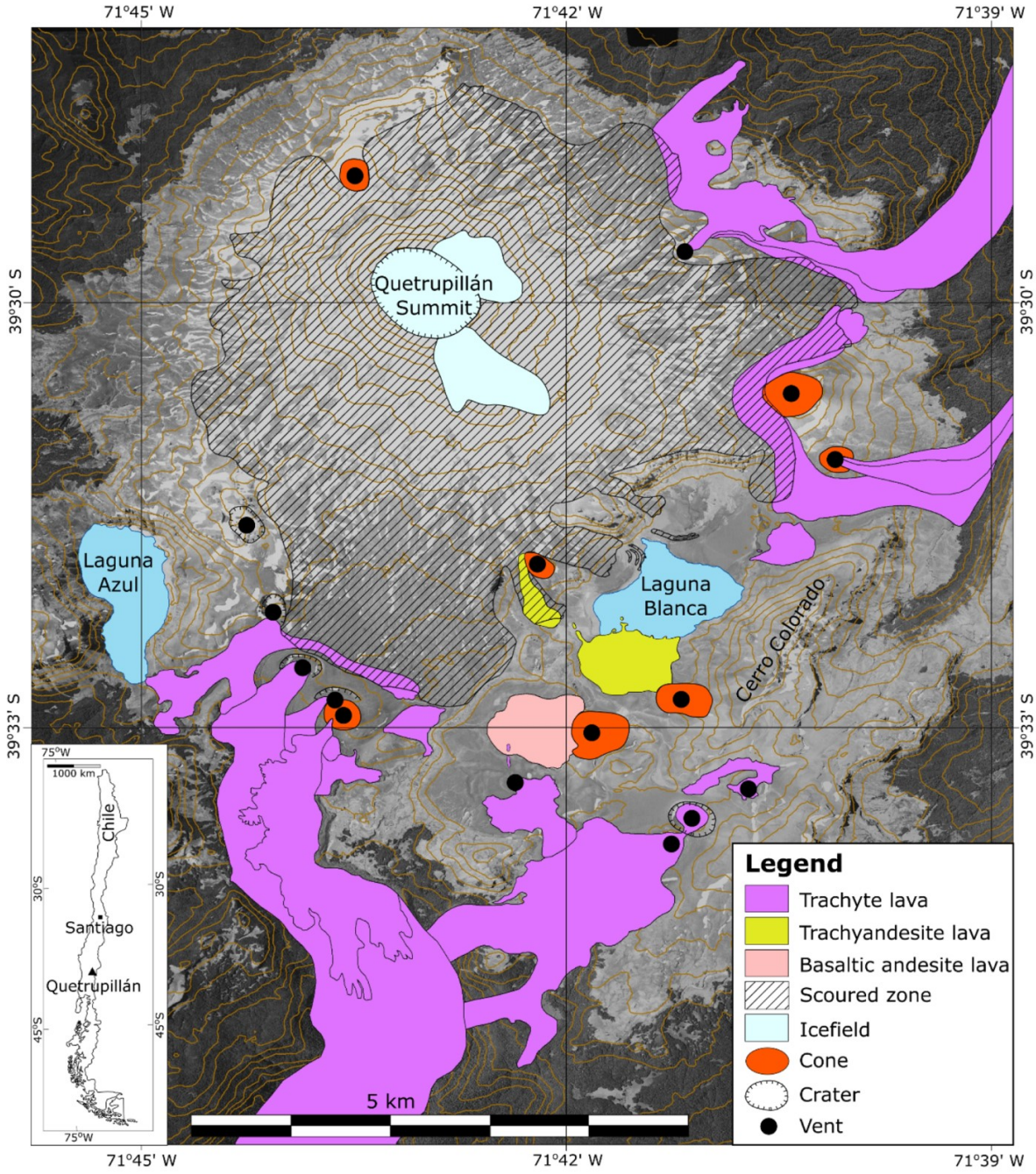
71°45' W
71°42' W
71°39' W
39°30' S
39°33' S
Quetrupillán
Summit
Laguna
Azul
Laguna
Blanca
Cerro Colorado
5 km
75°W
1000 km
Chile
30°S
45°S
Santiago
Quetrupillán
Legend
Trachyte lava
Trachyandesite lava
Basaltic andesite lava
Scoured zone
Icefield
Cone
Crater
Vent

Figure 2

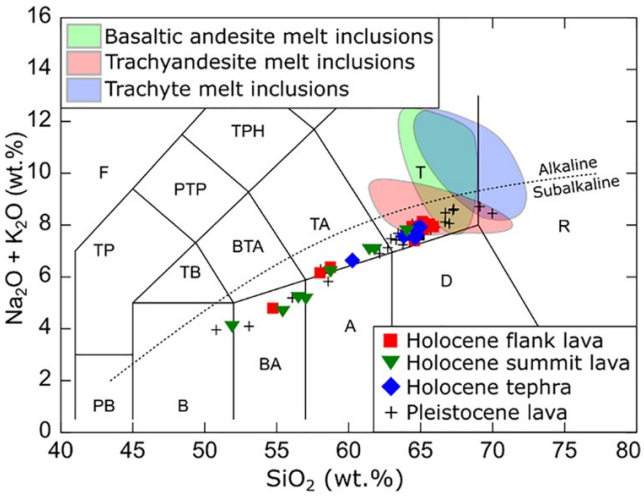
Basaltic andesite melt inclusions
Trachyandesite melt inclusions
Trachyte melt inclusions
TPH
F
PTP
T
Alkaline
Subalkaline
TA
R
TP
BTA
TB
D
A
BA
PB
B
Holocene flank lava
Holocene summit lava
Holocene tephra
Pleistocene lava
Na2O + K2O (wt.%)
SiO2 (wt.%)
0
2
4
6
8
10
12
14
16
40
45
50
55
60
65
70
75
80

Figure 3

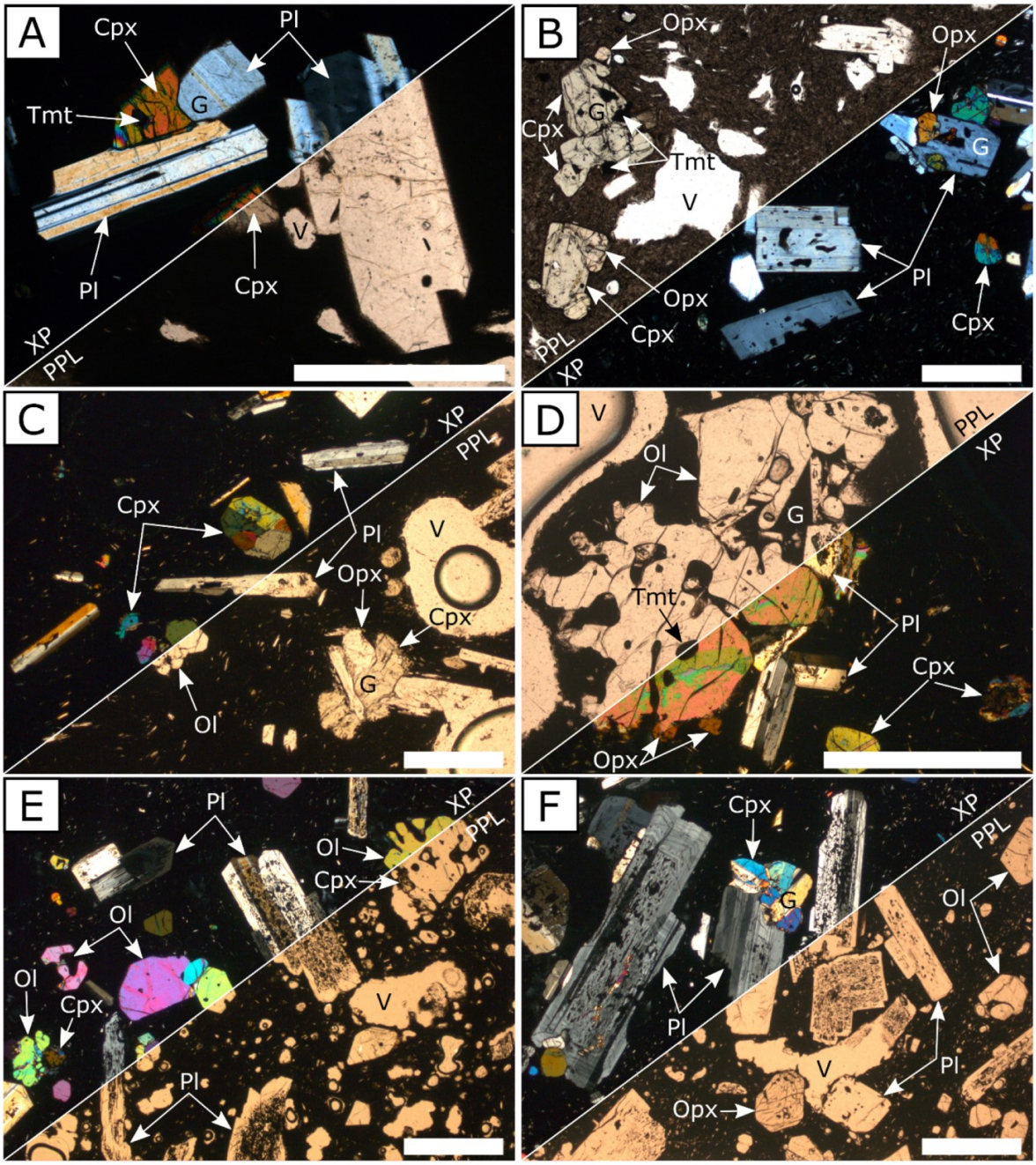
A
Cpx
Pl
Tmt
G
V
Pl
Cpx
XP
PPL
B
Opx
Opx
Cpx
G
Tmt
V
G
Pl
Opx
Cpx
Cpx
PPL
XP
C
XP
PPL
Cpx
Pl
V
Opx
Cpx
G
Ol
D
V
Ol
PPL
XP
G
Tmt
Pl
Cpx
Opx
E
Pl
XP
Ol
PPL
Cpx
Ol
Ol
Cpx
V
Pl
F
Cpx
XP
PPL
G
Ol
Pl
Pl
V
Opx

Figure 4

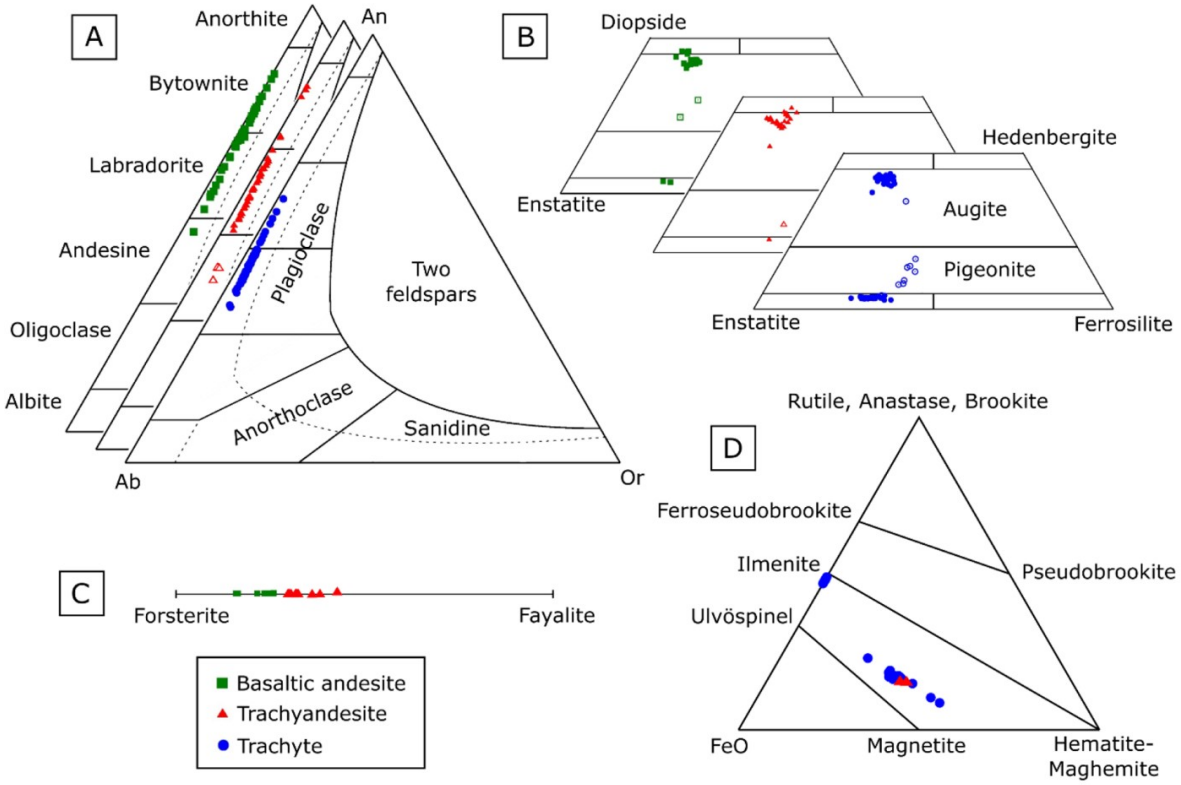
A
Anorthite
An
Bytownite
Labradorite
Andesine
Oligoclase
Albite
Plagioclase
Two
feldspars
Anorthoclase
Sanidine
Ab
Or
B
Diopside
Hedenbergite
Enstatite
Augite
Pigeonite
Enstatite
Ferrosilite
C
Forsterite
Fayalite
Basaltic andesite
Trachyandesite
Trachyte
D
Rutile, Anastase, Brookite
Ferroseudobrookite
Ilmenite
Pseudobrookite
Ulvöspinel
FeO
Magnetite
Hematite-
Maghemite

Figure 5

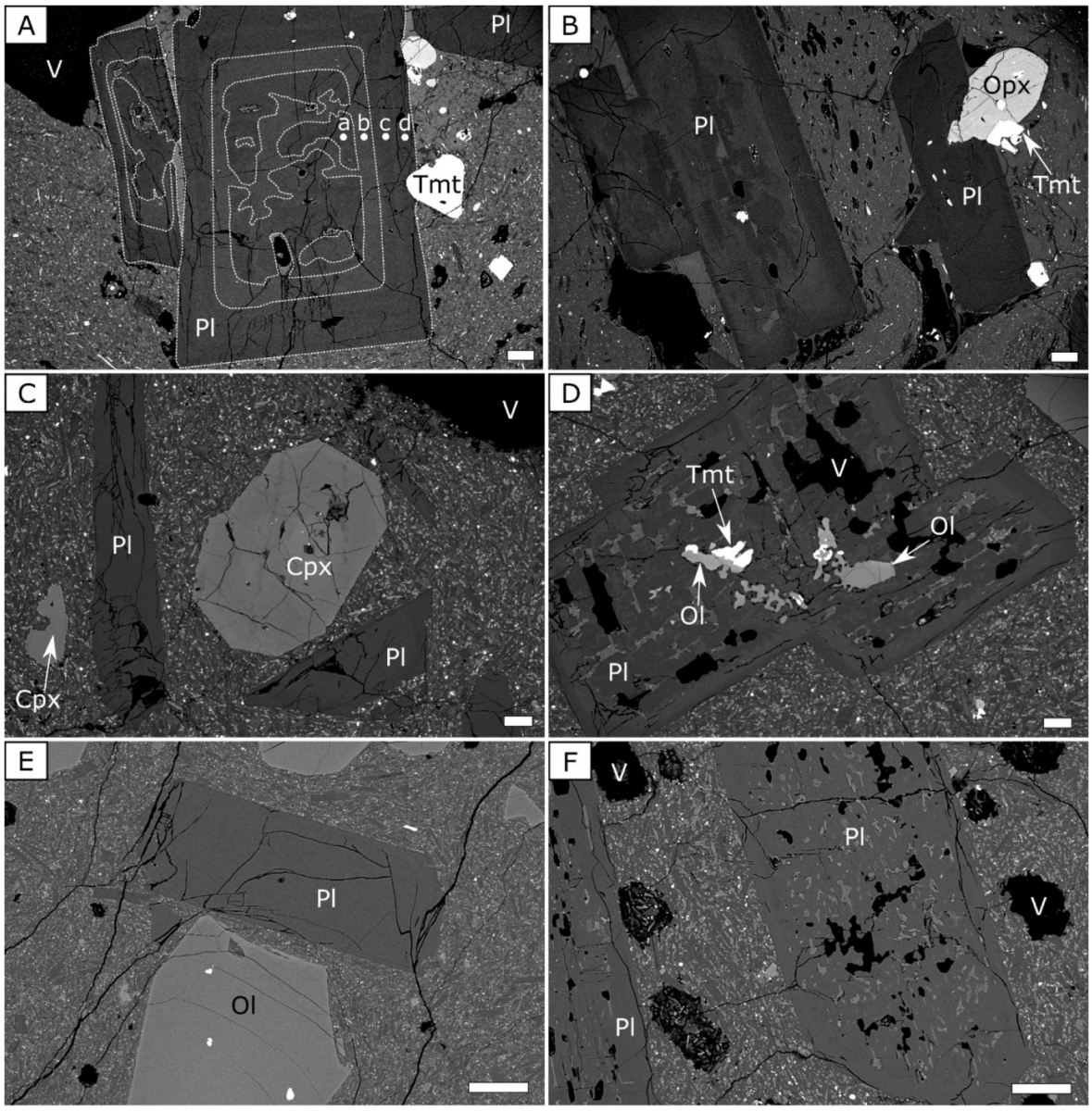
A
V
Pl
a b c d
Tmt
Pl
B
Pl
Opx
Tmt
Pl
C
V
Pl
Cpx
Pl
Cpx
D
Tmt
V
Ol
Ol
Pl
E
Pl
Ol
F
V
Pl
V
Pl

Figure 6

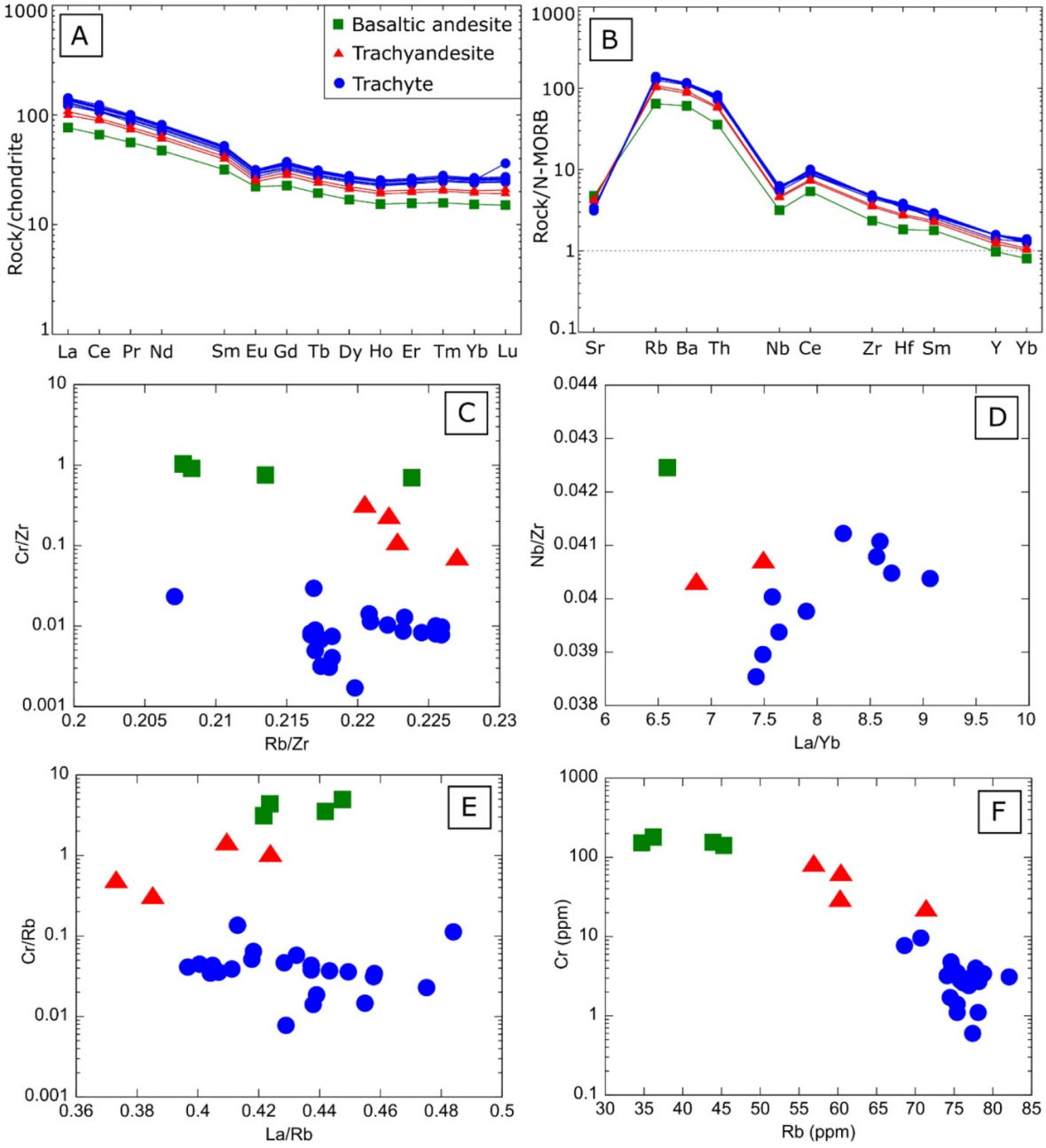
A
Basaltic andesite
Trachyandesite
Trachyte
Rock/chondrite
1000
100
10
1
La Ce Pr Nd Sm Eu Gd Tb Dy Ho Er Tm Yb Lu
B
Rock/N-MORB
1000
100
10
1
0.1
Sr Rb Ba Th Nb Ce Zr Hf Sm Y Yb
C
Cr/Zr
10
1
0.1
0.01
0.001
0.2 0.205 0.21 0.215 0.22 0.225 0.23
Rb/Zr
D
Nb/Zr
0.044
0.043
0.042
0.041
0.04
0.039
0.038
6 6.5 7 7.5 8 8.5 9 9.5 10
La/Yb
E
Cr/Rb
10
1
0.1
0.01
0.001
0.36 0.38 0.4 0.42 0.44 0.46 0.48 0.5
La/Rb
F
Cr (ppm)
1000
100
10
1
0.1
30 35 40 45 50 55 60 65 70 75 80 85
Rb (ppm)

Figure 7

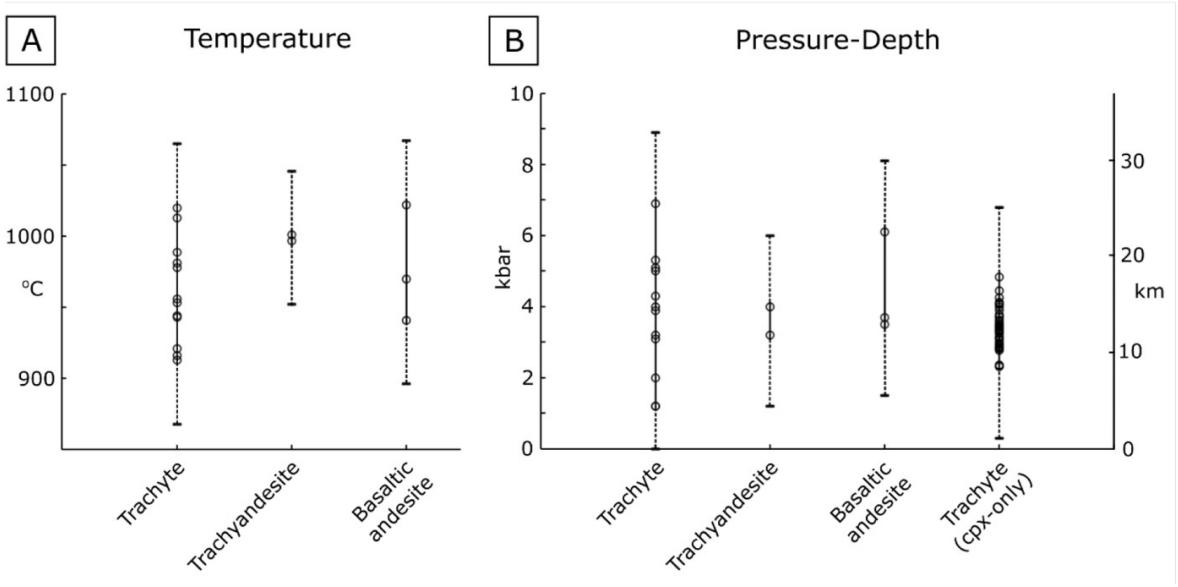
A
Temperature
1100
1000
°C
900
Trachyte
Trachyandesite
Basaltic andesite
B
Pressure-Depth
10
8
6
4
2
0
kbar
30
20
10
0
km
Trachyte
Trachyandesite
Basaltic andesite
Trachyte (cpx-only)

Figure 8

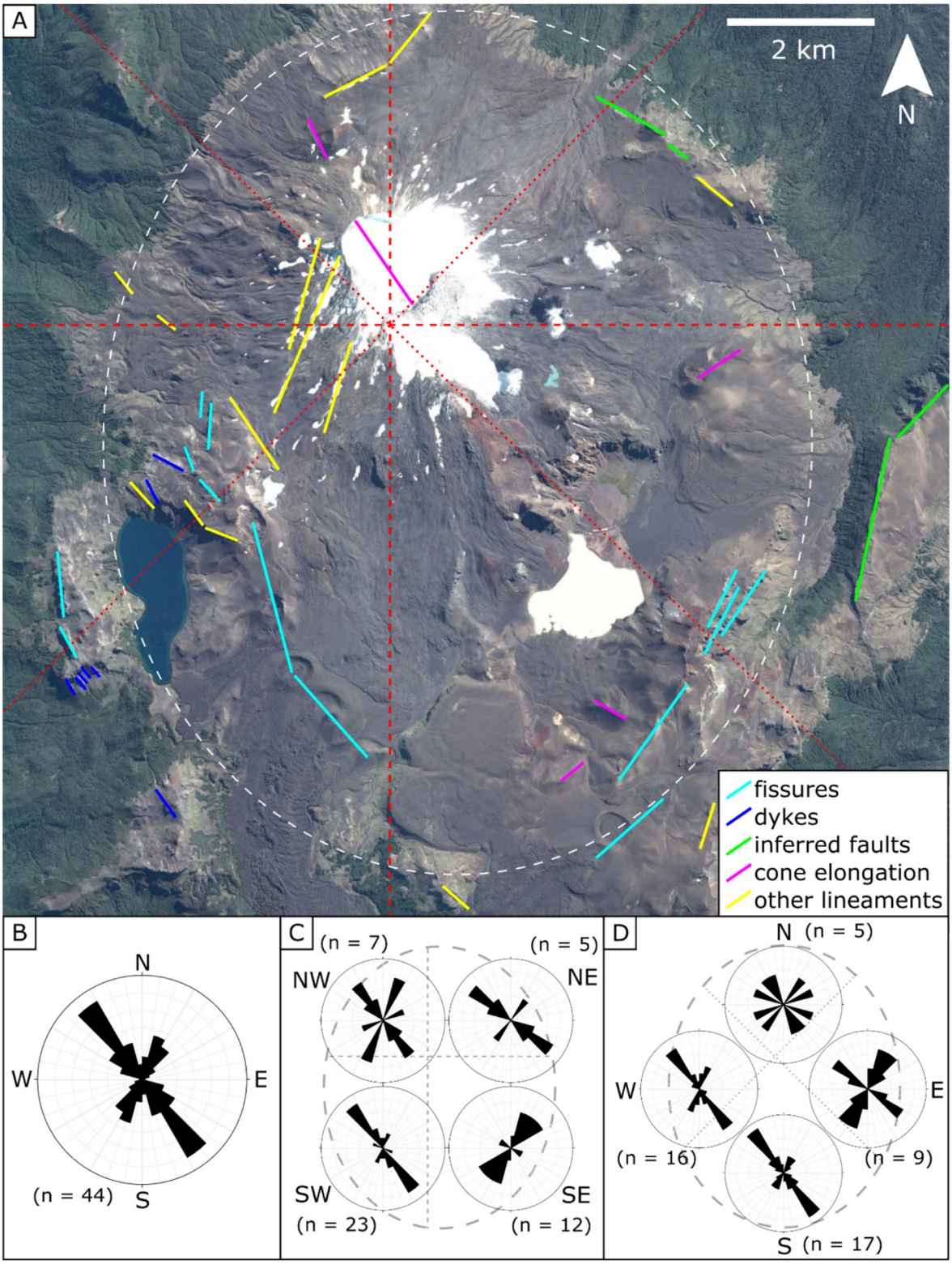
A
2 km
N
fissures
dykes
inferred faults
cone elongation
other lineaments
B
N
W
E
S
(n = 44)
C
(n = 7)
(n = 5)
NW
NE
SW
SE
(n = 23)
(n = 12)
D
N (n = 5)
W
E
(n = 16)
(n = 9)
S (n = 17)

Figure 9

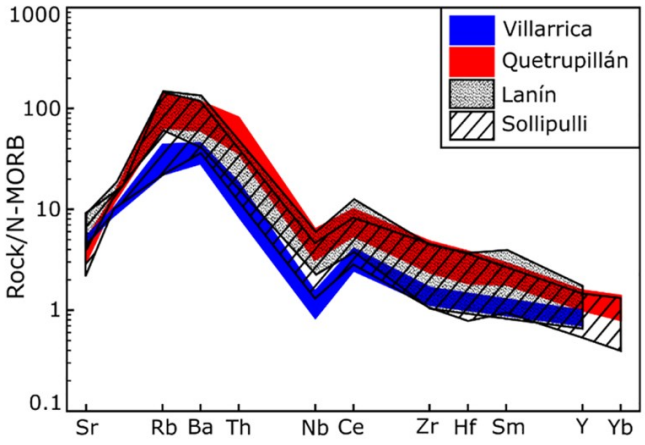
1000
100
10
1
0.1
Rock/N-MORB
Sr
Rb
Ba
Th
Nb
Ce
Zr
Hf
Sm
Y
Yb
Villarrica
Quetrupillán
Lanín
Sollipulli

Figure 10

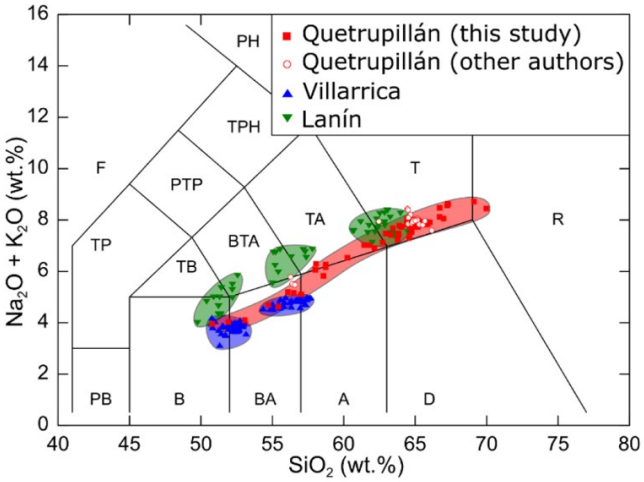
Quetrupillán (this study)
Quetrupillán (other authors)
Villarrica
Lanín
PH
TPH
F
PTP
T
TA
R
TP
BTA
TB
PB
B
BA
A
D
Na2O + K2O (wt.%)
SiO2 (wt.%)
0
2
4
6
8
10
12
14
16
40
45
50
55
60
65
70
75
80

Figure 11

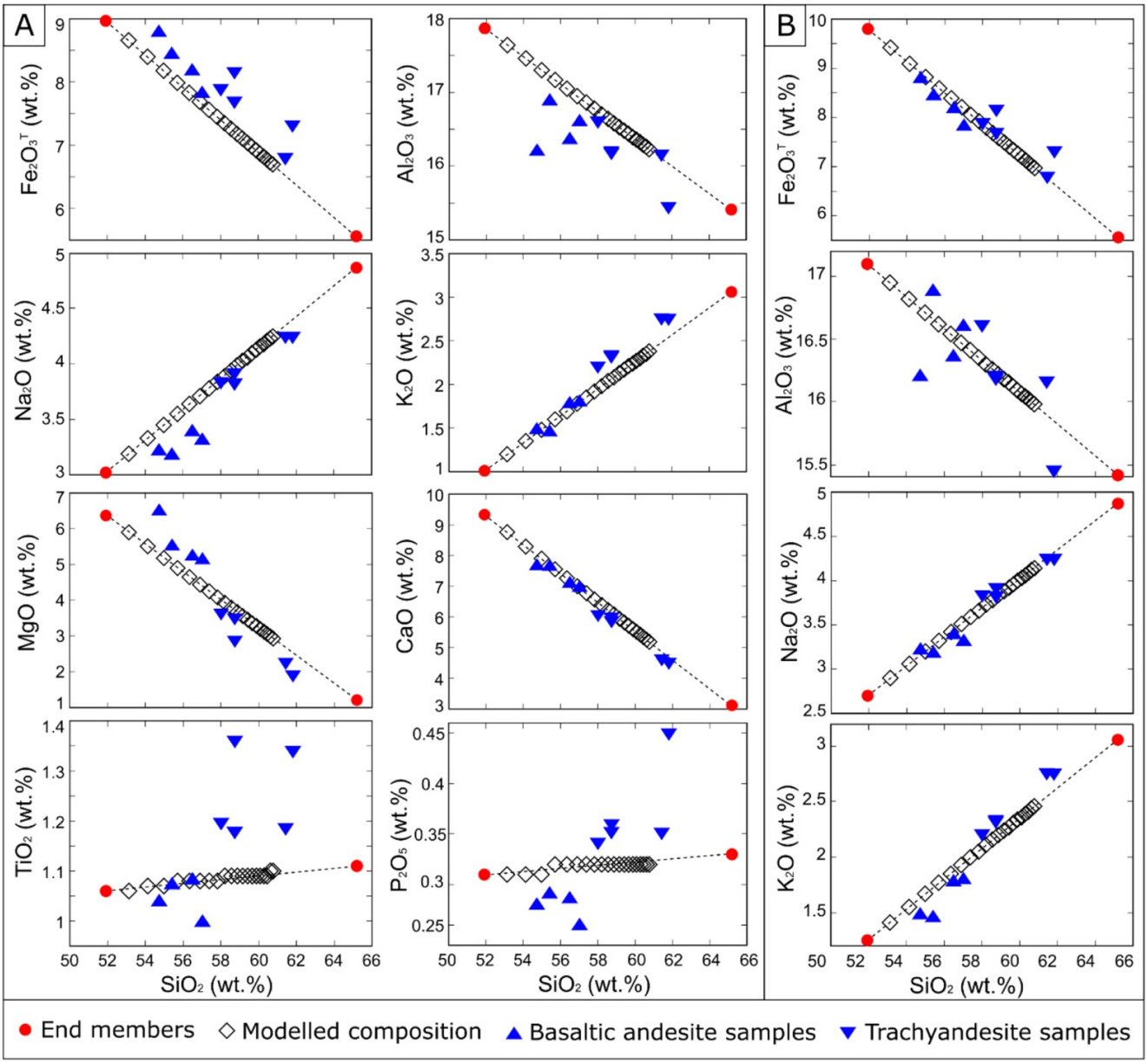
A
B
Fe2O3T (wt.%)
Al2O3 (wt.%)
Na2O (wt.%)
K2O (wt.%)
MgO (wt.%)
CaO (wt.%)
TiO2 (wt.%)
P2O5 (wt.%)
SiO2 (wt.%)
End members
Modelled composition
Basaltic andesite samples
Trachyandesite samples

Figure 12

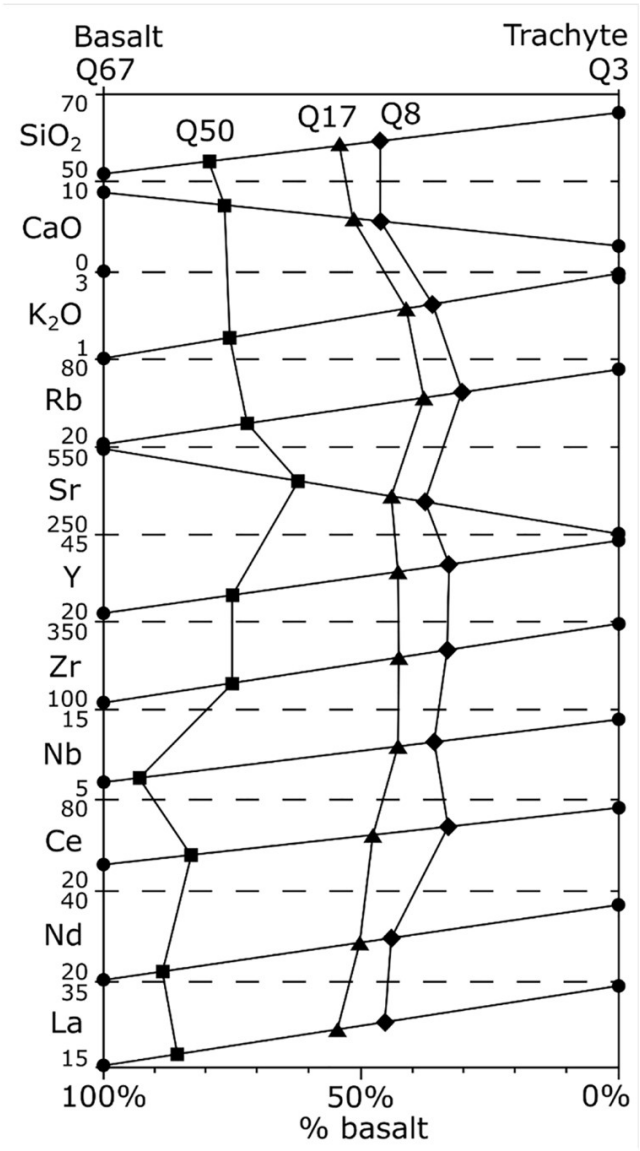
Basalt
Q67
Trachyte
Q3
Q50
Q17
Q8
SiO2
70
50
CaO
10
0
K2O
3
1
Rb
80
20
Sr
550
250
Y
45
20
Zr
350
100
Nb
15
5
Ce
80
20
Nd
40
20
La
35
15
100%
50%
0%
% basalt

Figure 13

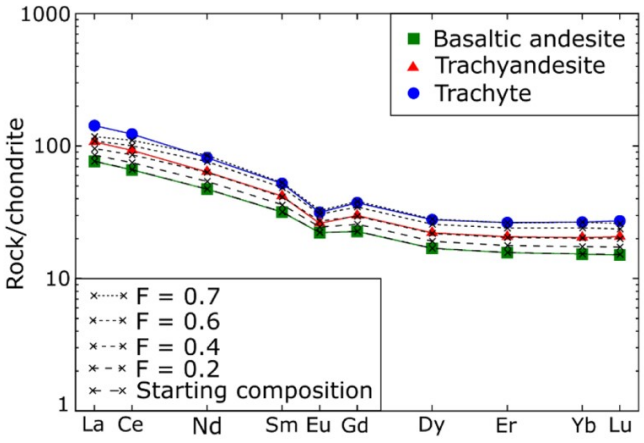
1000
100
10
1
Rock/chondrite
Basaltic andesite
Trachyandesite
Trachyte
F = 0.7
F = 0.6
F = 0.4
F = 0.2
Starting composition
La
Ce
Nd
Sm
Eu
Gd
Dy
Er
Yb
Lu

Figure 14

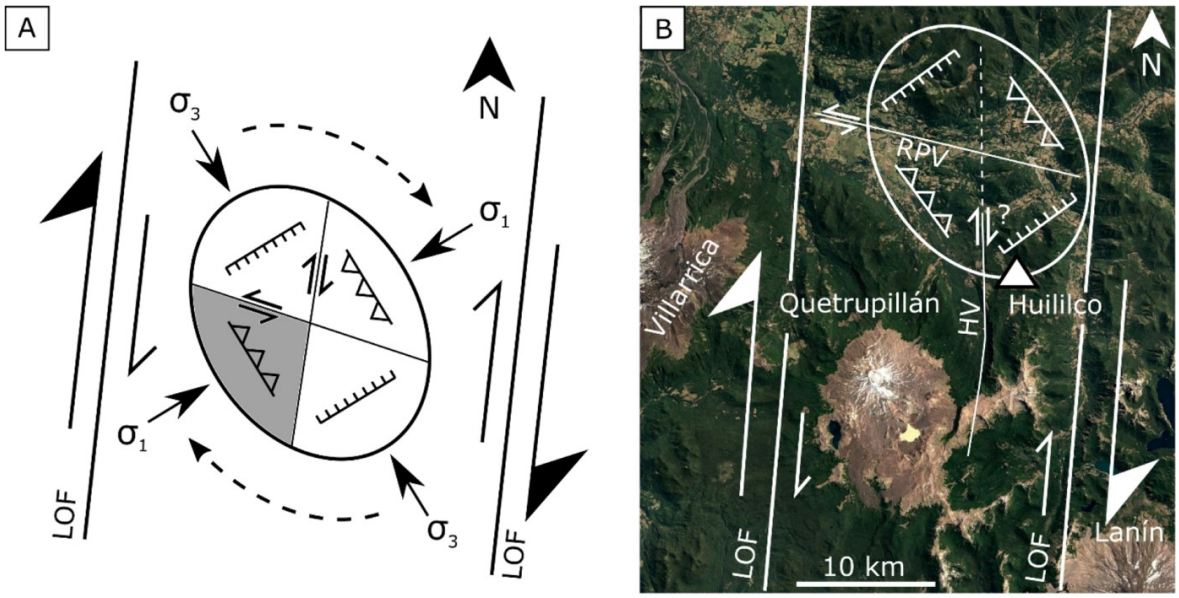
A
σ3
N
σ1
σ1
σ3
LOF
LOF
B
N
RPV
?
Villarrica
Quetrupillán
HV
Huililco
LOF
LOF
Lanín
10 km

Figure 15

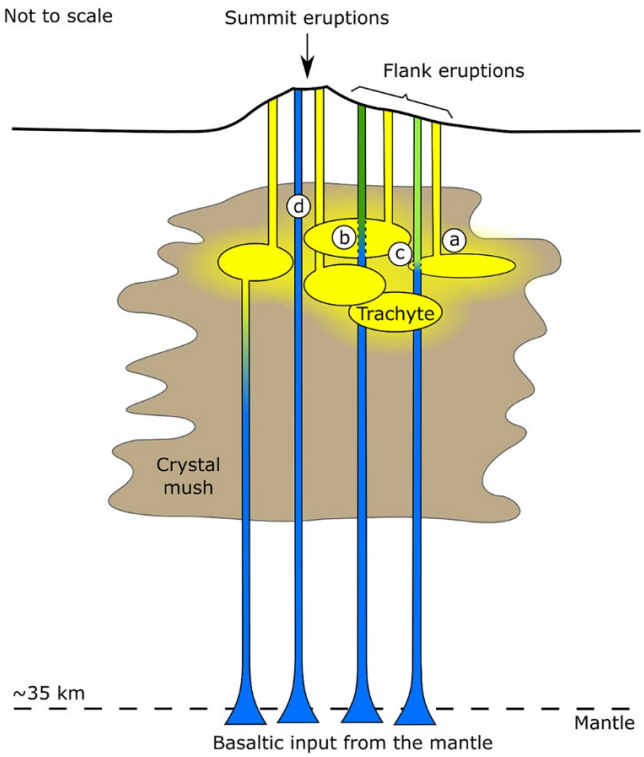
Not to scale
Summit eruptions
Flank eruptions
d
b
c
a
Trachyte
Crystal
mush
~35 km
Mantle
Basaltic input from the mantle

Figure 16